◆ Human Brain Mapping 2:165–189(1995) ◆

Spatial Registration and Normalization of Images

K.J. Friston, J. Ashburner, C.D. Frith, J.-B. Poline, J.D. Heather, and R.S.J. Frackowiak

The Wellcome Department of Cognitive Neurology, The Institute of Neurology, Queen Square, and the MRC Cyclotron Unit, London, United Kingdom

Abstract: This paper concerns the spatial and intensity transformations that map one image onto another. We present a general technique that facilitates nonlinear spatial (stereotactic) normalization and image realignment. This technique minimizes the sum of squares between two images following nonlinear spatial deformations and transformations of the voxel (intensity) values. The spatial and intensity transformations are obtained simultaneously, and explicitly, using a least squares solution and a series of linearising devices. The approach is completely noninteractive (automatic), nonlinear, and noniterative. It can be applied in any number of dimensions.

Various applications are considered, including the realignment of functional magnetic resonance imaging (MRI) time-series, the linear (affine) and nonlinear spatial normalization of positron emission tomography (PET) and structural MRI images, the coregistration of PET to structural MRI, and, implicitly, the conjoining of PET and MRI to obtain high resolution functional images.

Key words: realignment, registration, anatomy, imaging, stereotaxy, morphometrics, basis functions, spatial normalization, PET, MRI, functional mapping

INTRODUCTION

This paper is about the spatial transformation of image processes. Spatial transformations are both ubiquitous and important in many aspects of image analysis. For example, in neuroimaging, the realignment of a time-series of scans from the same subject (correcting for movement) is necessary for voxel-based analyses of time-dependent changes. This issue is of current interest in the analysis of functional magnetic resonance imaging (fMRI) time-series. Intersubject averaging, with change distribution analysis or statistical parametric mapping, requires the images to be transformed into some standard stereotactic space [e.g., Fox et al., 1988; Friston et al., 1991a]. Anatomical variability and structural changes due to pathology can be framed in terms of the transformations required to map the abnormal onto the normal. The interpretation of functional mapping studies often refers to some notion of normal anatomical variability [e.g., Steinmetz and Seitz, 1991]. This variability embodies neuroanatomical information of a probabilistic nature that is the focus of some important new brain mapping initiatives [e.g., Mazziotta et al., submitted].

Spatial transformations can be broadly classified as *label based* and *non-label based.* Label-based techniques identify homologous spatial structures, features, or landmarks in two images and find the transformation that best superposes the labelled points. These transformations can be linear [e.g., Pelizzari et al., 1988] or nonlinear (e.g., thin plate splines [Bookstein, 1989]). Non-label-based approaches identify a spatial transformation that minimizes some index of the difference

Received for publication July 28, 1994; revision accepted February 10, 1995.

Address reprint requests to Karl J. Friston, The MRC Cyclotron Unit, Hammersmith Hospital, DuCane Road, London W12 OHS, UK.

between an object and a reference image, where both are treated as unlabelled continuous processes. Again, these can be linear (e.g., principal axes [Alpert et al., 1990]; image realignment [Woods et al., 1992; Collins et al., 1994; and see Lange, 1994]) or nonlinear (e.g., plastic transformation [Friston et al., 1991b] with some interesting developments using neural nets [Kosugi et al., 1993].

In the absence of any constraints it is of course possible to transform any image such that it matches another exactly. The issue is therefore less about the nature of the transformation and more about defining the constraints under which the transformation is effected. The validity of the transformation can usually be reduced to the validity of these constraints. The first tenet of the general approach described here is that the constraints be explicit, reasonable, and operationally specified. The reliability of label-based approaches is limited by the reproducibility of the labelling. Non-label-based techniques are generally noninteractive and are therefore completely reliable. The second key aspect of our approach is therefore that it be non-label-based and automatic. Many approaches to spatial transformation use some form of gradient descent or nonlinear minimisation to find the global minimum of an error surface. These iterative techniques are flexible but may find local solutions and are computationally very expensive (e.g., 30 minutes for a simple linear MRI to MRI matching [Collins et al., 1994]). To avoid these problems we have used an approach with explicit and unique solutions that can be obtained by solving just one equation.

In short, the aim of this work was to develop an efficient, automatic, and general multidimensional nonlinear spatial transformation technique. (Rigid body and affine transformations were considered as special linear cases of this more general approach.) The only automatic nonlinear and noniterative technique used widely at present [Friston et al., 1991b] is fundamentally limited in the sense that it is only valid for one-dimensional images. (Current implementations apply this one-dimensional transformation to the radii of transverse slices in a polar space.)

This paper begins by describing the idea on which the transformations are based and providing the general operational equations. (A full exposition is provided in an appendix.) This is followed by a brief description of the fMRI, structural MRI, and positron emission tomography (PET) data used in subsequent sections. The remaining four sections deal with a range of specific applications and extensions. The first ("Within modality, within subject") illustrates the simplest application, namely, orthogonal (rigid body) transformations of single-slice fMRI data that would be applied to reduce head movement artifact in fMRI time-series. The algorithm was tested using simulated head movement and a real time-series of 64 images. Performance was assessed by comparing the estimated and known movement parameters. The estimates were also compared with those obtained with a widely used image realignment routine [Woods et al., 1992]. Using a real time-series, the validity of the realignment was further addressed by looking at its effect on time-dependent functional changes. The second section ("Within modality, between subject") deals with general nonlinear three-dimensional transformations of the sort required to map an arbitrary PET image into a standard PET image conforming to the space described by the atlas of Talairach and Tournoux [1988]. This spatial normalization transformation is used to 1) introduce a recursive application of the least squares analysis and 2) compare it with equivalent nonlinear minimisation. The section concludes by introducing a simultaneous solution for the transformation using a series of feature-enhanced images derived from the primary image pair. This extension is demonstrated in the context of matching structural MRI images from different subjects. The third section ("Between modality, within subject")

Table of Symbols

$\dagger(x)$ and $\dagger$	The image designated the template or reference image
$\Omega(x)$ and Ω	The image designated the object or observed image
$f_x\{.\} = c(x) * \gamma_x(.)$	The operator mapping voxel values from reference to object at x
$c(x)$ and $\mathbf{c}$	The convolution kernel or matrix
$\gamma_x(.) = \Sigma u_i(x).f^i\{.\}$	The nonlinear functional component of $f_x\{.\}$ at x
$f^i\{.\}$	The ith function in the expansion of $\gamma_x(.)$
$u\times i(x) = \Sigma u_{ij}\beta_j^f(x)$	The ith coefficient of the expansion of $\gamma_x(.)$ at x
u_{ij} and $\mathbf{u}_i$	The coefficients of the expansion of $u_i(x)$ in space (an unknown)
$\beta_j^f(x)$ and $\boldsymbol{\beta}^f$	The spatial basis functions of the expansion of $u_i(x)$ in space
$q(x) = x + \Sigma q_k\beta_k^q(x)$	The function describing the spatial transformation or movement
$\beta_k^q(x)$ and $\boldsymbol{\beta}^q$	The spatial basis functions of $q(x) - x$
q_k and $\mathbf{q}$	The coefficient of the expansion of q(x) (an unknown)
$\partial\Omega(x)/\partial x$ and $\partial\Omega/\partial\mathbf{x}$	The derivative of the object with respect to x
$\partial\Omega(q(x))/\partial q_k$ and $\partial\Omega/\partial\mathbf{q}$	The derivative of the object with respect to q_k

looks at the registration of structural MRI and PET from the same individual. The focus here is on the intensity transformation implicit in the overall solution. This intensity transformation can be used to create a structural MRI image whose voxel values are functional [e.g., regional cerebral blood flow (rCBF)-like] in nature. The final section ("Between modality, between subject") deals with the most general problem of normalization using structural MRI and functional PET images from different subjects.

This paper is methodological; however, its main aim is to communicate the basic idea, mathematical formalism, and the variants or extensions that ensue. The focus is therefore more conceptual than operational. Subsequent papers will present more detailed numerical information on performance, robustness, and application to some simple questions about normal and abnormal anatomical variability.

THEORY

The basic idea is to formulate the most general problem of spatial transformation so that a unique least squares solution exists. This involves linearising a highly nonlinear multidimensional problem using reasonable constraints. This linearisation starts by acknowledging that the differences between two images [say $\Omega(x)$ and $\dagger(x)$] have two components: The first component is due to voxel value or intensity differences when two images are in perfect anatomical register. These differences may be artifactual (e.g., different resolutions, low spatial frequency intensity variations in MRI images or different methods of rCBF parameter estimation used for PET) or real (e.g., hypofrontality in PET scans of psychomotor poverty syndromes, differences in global activity, or experimentally induced physiological activations). We assume that, at point x, there is some operator $f_x\{.\}$ that transforms voxel values from one image to those of another (assuming perfect anatomical congruence).

The second component of the differences between the two images will be due to misalignment or indeed differences in shape and size of the objects scanned. This spatial discrepancy between the two scans is assumed to be characterized by a function of position $q(x)$. This partitioning of the difference between one image and another can be expressed as:

$$f_x\{\dagger(x)\} = \Omega(q(x)) + e(x) \qquad (1)$$

where $e(x)$ is some error. For simplicity this error term will be omitted in subsequent expressions. Equation (1) expresses the conjecture that two images can be approximated by applying an *intensity transformation* $f_x\{.\}$ to one and a *spatial transformation* $q(x)$ to the other. The next step is to linearise Equation (1) so that both $f_x\{.\}$ and $q(x)$ have explicit least squares solutions. This can be effected by low order approximations and by imposing some constraints on the forms of $f_x\{.\}$ and $q(x)$. The constraints are basically 1) that the operator $f_x\{.\}$ can be expressed in terms of a convolution and a (nonstationary) nonlinear function and 2) that both $f_x\{.\}$ and $q(x)$ change slowly with location. For $f_x\{.\}$ this local-stationariness means that the "operation" that converts voxel values from one image into the other (the intensity transformation) can change with position but is similar within a given locale. In other words, the transformation $f_x\{.\}$ is locally stationary but globally unspecified. Stationariness means that something does not change with position in the image. The slowly changing nature of $q(x)$ means that the spatial transformation is smooth and that local contiguity relationships are preserved. More formally, the smooth spatial transformation ensures a positive Jacobian which preserves important features, including critical points such as peaks and saddle points [Amit et al., 1991]. Stronger constraints can be imposed on $q(x)$, for example in realigning scans from the same individual, $q(x)$ would represent an orthogonal rigid-body transformation with six parameters, but would still be smooth.

In what follows $f_x\{.\}$ is taken to be some nonlinear function $\gamma_x(.)$ of the original process convolved with a kernel $c(x)$. This means that, ignoring misregistration effects, one image can be converted into another by applying a nonlinear transformation to the voxel values and then (de-)convolving into the same resolution as the second image, i.e., $f_x\{.\} = c(x) * \gamma_x(.)$ where $*$ means convolution. Note that this form of $f_x\{.\}$ requires the nonlinear function to be applied before the convolution. In practice one would always want to arrange the images so that one was convolving the higher resolution image to match the lower resolution image. The kernel or differential point spread function $c(x)$ will be known or can be estimated post hoc using established and empirical methods of estimating image smoothness [Friston et al., 1991a]. Without loss of generality one can take some expansion of $\gamma_x\{.\} = \Sigma\, u_i(x).f^i(\dagger(x))$ and expand the position-dependent coefficients $u_i(x)$ in terms of some "smooth" spatial basis functions $\beta_j^f(x)$ [i.e., $u_i(x) = \Sigma\, u_{ij}\beta_j^f(x)$]. An expansion is simply expressing a function as the sum of (usually) simpler functions. $q(x)$ can be similarly expanded in terms of x and some smooth basis functions $\beta_k^q(x)$. Smooth basis functions can be thought of as

smooth functions of, or profiles in, space that are (usually) chosen to be independent or orthogonal. Using these expansions Equation (1) becomes:

$$c(x) * \Sigma\{f^i(\dagger(x)) \Sigma u_{ij}\beta_j^f(x)\} \approx \Omega(x + \Sigma q_k\beta_k^q(x)). \quad (2)$$

Now if $\Omega(x)$ is smooth the effects of small distortions $q_k\beta_k^q(x)$ will not interact to a significant degree. In other words, if $\Omega(x)$ is smooth we can expand the right-hand side of Equation (2) using Taylor's theorem where, ignoring high order terms:

$$\Omega(x + \Sigma q_k\beta_k^q(x)) \approx \Omega(x) + \Sigma q_k\partial\Omega/\partial q_k \quad (3)$$

(see Appendix). Combining Equation (2) and Equation (3) we get:

$$\Sigma\Sigma u_{ij}[c(x) * f^i(\dagger(x)).\beta_j^f(x) \approx \Omega(x) + \Sigma q_k\partial\Omega/\partial q_k. \quad (4)$$

This approximate equality says that, give or take some residual error, one image can be approximated to another by 1) applying an intensity transformation to the first image (where the coefficients of the transformation's expansion can change slowly with position) convolving, and 2) approximating the distortion of the second image by simply adding the effects of each component of the distortion (assuming the components are small relative to the image's resolution). The components of the distortion are defined by a set of smooth basis functions in space.

The importance of Equation (4) is that it is linear in the unknown coefficients (u_{ij} and q_k) and that these coefficients have a unique least squares solution. This may be seen more clearly by considering the matrix equivalent of Equation (4) which is of the form $\mathbf{A}.[\mathbf{u}_0\,\mathbf{u}_1 \cdots \mathbf{q}]^T \approx \Omega$:

$$[\mathbf{c}.\mathrm{diag}(f^0(\dagger)).\boldsymbol{\beta}^f\ \mathbf{c}.\mathrm{diag}(f^1(\dagger)).\boldsymbol{\beta}^f \cdots - \mathrm{diag}(\partial\Omega/\partial\mathbf{x}).\boldsymbol{\beta}^q].[\mathbf{u}_0\,\mathbf{u}_1 \cdots \mathbf{q}]^T \approx \Omega \quad (5)$$

(see Appendix for a fuller explanation and notational details). The vector $[\mathbf{u}_0\,\mathbf{u}_1\,\mathbf{u}_2 \cdots \mathbf{q}]$ has a unique least squares solution. This solution for q_k ($\mathbf{q}$) can then be used to implement the spatial transformation that maps $\Omega(x)$ onto $\dagger(x)$ or vice versa given that $q(x) = x + \Sigma q_k\beta_k^q(x)$.

THE DATA

This section describes briefly how the data were acquired and stored. The data were obtained from (different) male subjects in accord with local and national ethical requirements.

Functional MRI data

The data were a time-series of 64 gradient-echo EPI coronal slices (5 mm thick, with 64 × 64 voxels) through the calcarine sulcus and extrastriate areas. Images were obtained every 3 seconds from a normal male subject using a 4.0-T whole-body system, fitted with a small (27 cm diameter) z-gradient coil (TE, 25 ms; acquisition time, 41 ms). Photic stimulation (at 16 Hz) was provided by goggles fitted with 16 light emitting diodes. The stimulation was off for the first 10 scans (30 s), on for the second 10, off for the third, and so on. The data were interpolated to 128 × 128 voxels. The image dimensions were 128 × 128 × 1. The voxel size was 1.25 × 1.25 × 5 mm. Data were stored at 8-bit precision.

Structural MRI data

These data were high resolution structural MRI scans obtained at 1.5 T using a standard T1-weighted sequence. The image dimensions (following reorientation of the sagittal acquisition and resampling) were 256 × 256 × 118. The voxel size was 0.976 × 1.3 × 1.952 mm. Data were stored at 8-bit precision.

PET data

The PET images were obtained with a CTI PET camera (model 953B, CTI, Knoxville, TN, USA). Reconstructed images had a resolution of about 8 mm [Townsend et al., 1992; Spinks et al., 1992]. ^{15}O was administered intravenously as radiolabelled water infused over 2 minutes. Total counts per voxel during the buildup phase of radioactivity served as an estimate of rCBF [Fox and Mintun, 1989]. The image dimensions (following reconstruction and bilinear interpolation) were 128 × 128 × 43. The voxel size was 2.09 × 2.09 × 2.45 mm. Data were stored at 8-bit precision.

All the image manipulations and matrix calculations were performed in MATLAB (MathWorks Inc., Sherborn, MA, USA) on a SPARC Workstation. The PET and MRI images were scalp edited. (Preprocessing of this sort is not a prerequisite for anything that follows.)

APPLICATIONS

Within subject, within modality

In this section we deal with one of the simpler transformations, namely, the registration of homolo-

gous images acquired sequentially from the same subject. This application is important because it removes variance from time-series that would otherwise be attributed to error (i.e., decreasing sensitivity) or to treatment effects (i.e., movement artifacts). The most important source of this variance is usually movement during the scanning session. Although important in PET studies, these effects can seriously confound the analysis of fMRI studies, where the slightest subvoxel movement may profoundly effect the voxel value. This section is divided into two parts. In the first we compare the least squares approach to known (simulated) movement and to that estimated with a widely used image realignment program (automated image realignment [AIR] [Woods et al., 1992]). In the second part the least squares approach is applied to the real fMRI time-series to demonstrate that the estimated movement is real and to validate the realignment in terms of detecting functional changes. This is achieved by analyzing the fMRI time-series using singular value decomposition (SVD). SVD identifies important spatial modes and their time-dependent activity.

The reason realignment can be considered a simple case of the more general spatial transformation problem is because the form of the spatial transformation q(x) is exactly specified and the intensity transformation is known $f_x\{\dagger(x)\} \approx \dagger(x)$. The second equality follows from the fact that the same object is scanned with the same imaging device. (We are obviously assuming that time-dependent physiological changes of interest are small relative to the anatomic profile and that these effects can be relegated to the error term.) Substituting these simple forms for q(x) and $f_x\{.\}$ into Equation (4), one has (in matrix notation):

$$[-\mathrm{diag}(\partial\Omega/\partial\mathbf{x}).\boldsymbol{\beta}^q].\mathbf{q}^T \approx [\Omega - \dagger]$$

or

$$-\partial\Omega/\partial\mathbf{q}.\mathbf{q}^T \approx [\Omega - \dagger]. \qquad (6)$$

In this instance the basis functions cover the space of all allowable translations and rotations, i.e., $\boldsymbol{\beta}^q = [\beta_1^o\ \beta_2^o \cdots\cdots \beta_6^o]$ where the columns β_k^o correspond to translations in three dimensions and the three orthogonal rotations. In practice it is easier to compute the six columns of $\partial\Omega/\partial\mathbf{q}$ directly [as implied in the second form of Equation (6)] by simply applying small translations and rotations to Ω(x) and measuring the changes in voxel values. The six elements of the row vector **q** correspond to the estimated translations and rotations that constitute the movement to be corrected.

Simulated movement

The first fMRI slice was translated over 64 logarithmically increasing distances (1 μm to 3 mm) and the displacement was estimated for each simulated movement by comparing the moved image and the first or reference image. These estimates were computed with least squares according to Equation (6) and the appropriate AIR algorithm. Moved images were constructed by adding uncorrelated Gaussian noise (at 5% of the image mean), to emulate the effects of thermal noise in the fMRI scans, and translating with bilinear interpolation. Clearly this is not the same as actually moving the real object but is a reasonable approximation for small movements. The data were saved as 8 bit. This reduction to 8-bit precision introduces nonlinear noise due to round-off errors and to some extent simulates digitizing noise during acquisition. The actual and estimated translations were compared graphically.

Figure 1 presents the results of this analysis. These results highlight two points. First, both the AIR and the least squares estimates are generally very good. This sort of analysis helps to establish the construct validity of both techniques in terms of the other. Second, at very large and small displacements, there is a dissociation in the performance of the two techniques. AIR is better than the least squares approach when the spatial misalignment approaches the resolution of the images (~2.5 mm). The upper line (in Fig. 1, left) represents the actual movement and the AIR estimates. The lower line corresponds to the least squares estimates. This divergence at large translations is due to a failure of the first order approximation of the Taylor series implicit in Equation (3); more simply, if the displacements are bigger than the image's smoothness then the linearisation in the least squares approach becomes suspect. In practice this is not a problem because 1) the images can be smoothed, or 2) the least squares analysis can be applied recursively (see below). Conversely, the least squares analysis is better for small displacements. Figure 1 (right) shows the same data but on a semilog scale. The AIR algorithm starts to fail noticeably at about 100 μm whereas the least squares analysis remains reasonably robust until about 10 μm.

The differences between the least squares and AIR estimates should not be overinterpreted in the sense that many differences were not controlled for in the two algorithms. In general, results obtained from the two analyzes are consistent. It should be noted, however, that the least squares analysis is about an order of magnitude faster than the AIR. This is because the AIR approach is iterative.

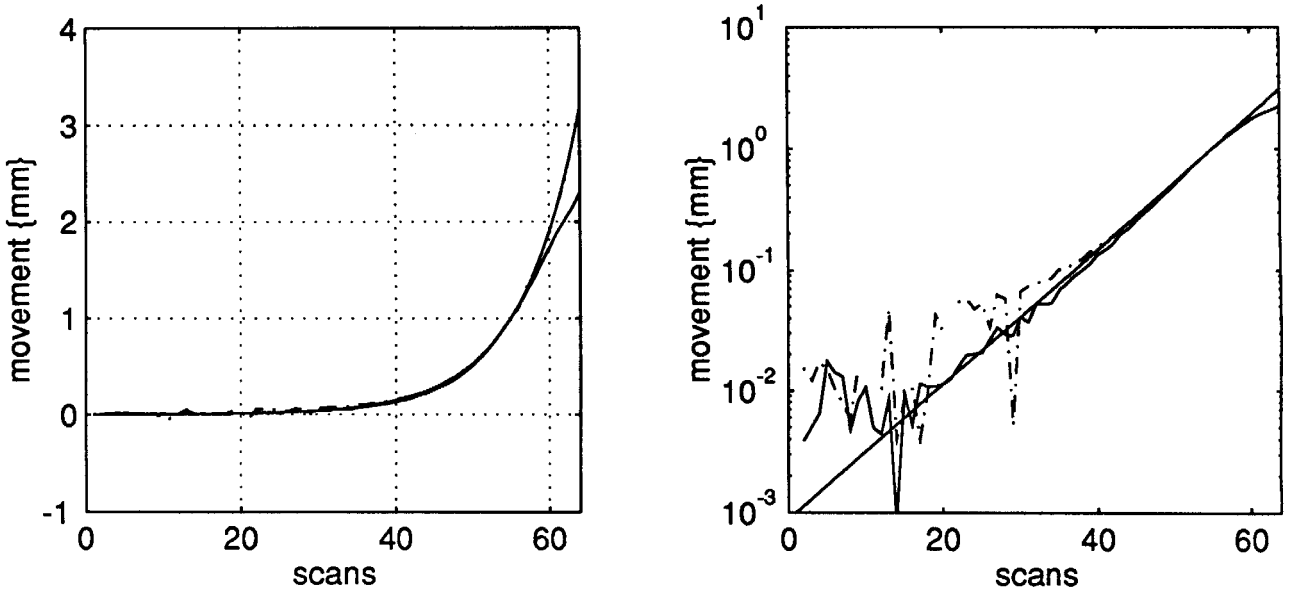

Figure 1.

Comparison of the least squares technique with known (simulated) movement parameters and parameter estimates using AIR [Woods et al., 1992]. **Left:** y translation expressed in millimeters over the different simulated movements. The two solid lines correspond to the actual and least squares estimates of movement. The least squares estimate deviates on the extreme right (lower curve) from actual movement. The AIR estimates (broken line) are largely superimposed on the actual movement curve. **Right:** The same data plotted on a semilog scale. Straight line, actual; solid line, least squares; broken line, AIR.

A real time-series

It may seem to some that a precision of 100 μm or less is rather irrelevant for realignment routines because this scale of movement is practically undetectable and harmless anyway. They would be wrong. The purpose of this section is to show that 1) movements measured in tens of micrometers can be detected in fMRI time series, and 2) removal of these effects by realignment can substantially effect the variance-covariance structure of the data.

The 64-scan time-series was subject to the least squares analysis using the first scan as a reference. The movement parameters reflecting estimated movement suggested translations (solid lines in the upper panel of Fig. 2) in the order of 100 μm or less. These translations will be referred to as Δx and Δy. The results of this analysis compared well with the equivalent AIR results (see the lower panel of Fig. 2).

To demonstrate that these estimated movements were due to real movement, the time-dependent hemodynamic variance was partitioned into a series of orthogonal spatial modes (or eigenimages) using SVD (the first four scans were ignored to avoid magnetic saturation effects). See Friston et al. [1994] for a discussion of spatial modes and their identification. In brief, these spatially distributed patterns reflect independent systems that share a common source of variance. Figure 3 (top right) shows the first spatial mode (that accounting for the most variance). This mode has been elicited by photic stimulation and includes striate and extrastriate regions. The time-dependent expression of this mode (the solid line in the top left of Fig. 3) matches that predicted by photic stimulation (the dotted line). The dynamics predicted by photic stimulation were obtained by convolving the square wave input with a hemodynamic response function of 7 seconds delay and dispersion [Friston et al., 1994].

Consider now the third mode—that accounting for the third largest source of variance. (The second mode is not shown in this paper.) Inspection of the third mode immediately suggests that it can be attributed to movement along a positively inclined diagonal. Figure 3 (bottom right) shows that the time-dependent expression of the third mode (solid line) is closely matched by least squares estimates (Δx and Δy) of diagonal motion $1.3.\Delta x + 1.7.\Delta y$ (dotted line). This concordance demonstrates that movements estimated by the least squares analysis are probably real.

The relative contribution of the first and third spatial modes can be expressed in terms of the appro-

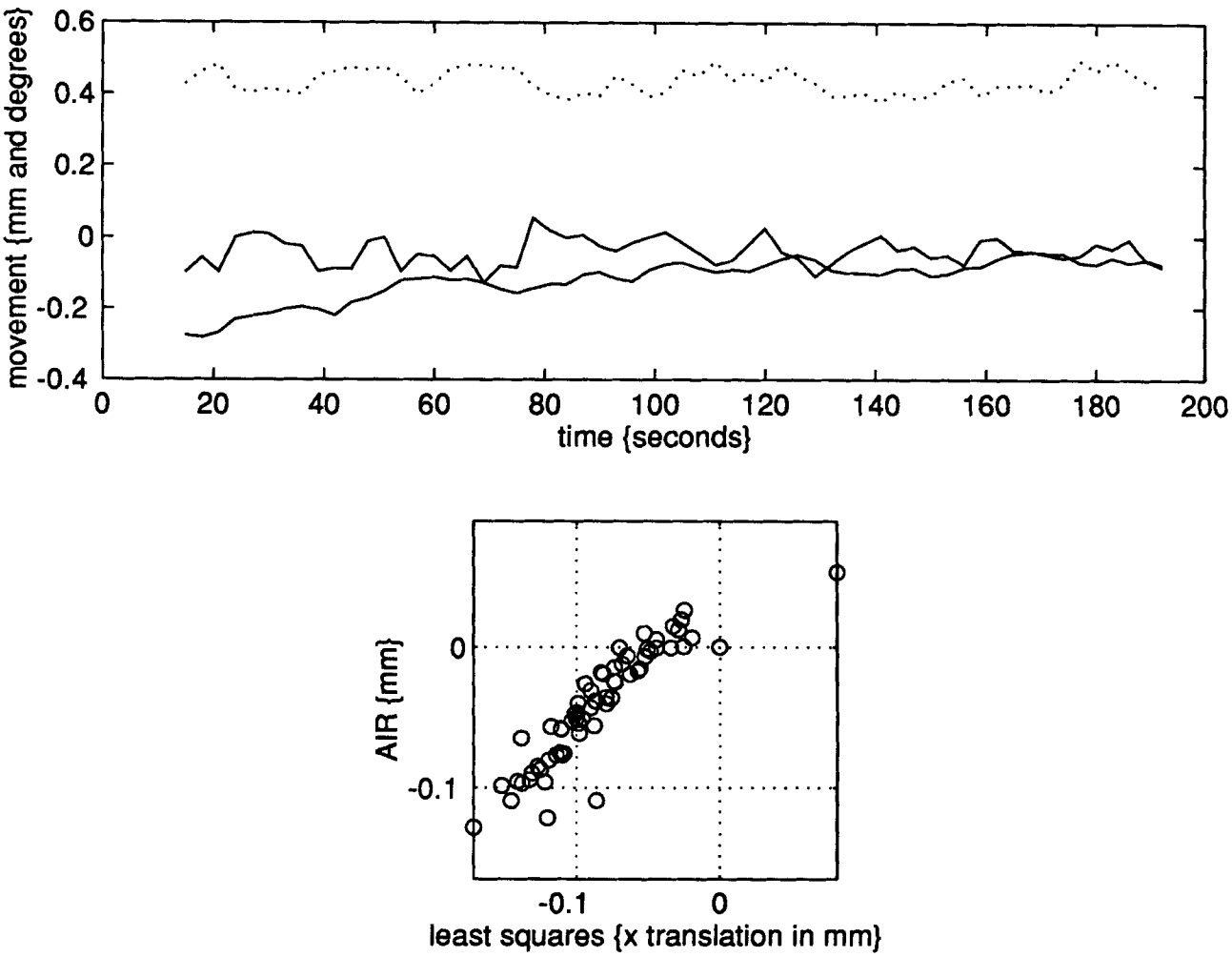

Figure 2.
Estimated movement from a real time-series of 64 coronal fMRI slices through visual cortex. **Upper panel:** x and y translation (solid lines) and rotation (broken line) as estimated by the least squares approach. **Lower panel:** x translation estimated using AIR regressed on least squares estimates.

priate 2-norm (a standard measure of how much a pattern or vector of voxel values contributes to the variance–covariance structure). For the original data these 2-norms are the eigenvalues associated with the spatial modes and are presented in Figure 4 (left). The remarkable observation is that variance due to subject movement (of usually less than 100 μm) was about one-seventh of that introduced by the sensory stimulation. It is pleasing to see that this, and only this, source of variance (the third mode) was reduced following realignment of the images (Fig. 4, right).

It may be asked at this point: "why not simply remove this mode from the time-series?" Or, more generally: "why not remove any component of all the modes that corresponds to a partial spatial derivative of the image?" In fact, this is equivalent to the least squares approach proposed.

Within modality, between subject

In this section we consider the more general problem of spatial transformation where the same imaging device has been used but the objects imaged (e.g., subjects' heads) are not exactly the same. Spatial or stereotactic normalization belongs to this class of problems when it is solved by matching an arbitrary image to some ideal image, model, or template. For example, in the intersubject averaging of PET activation studies, change distribution analysis [Fox et al., 1988] and statistical parametric mapping [Friston et al.,

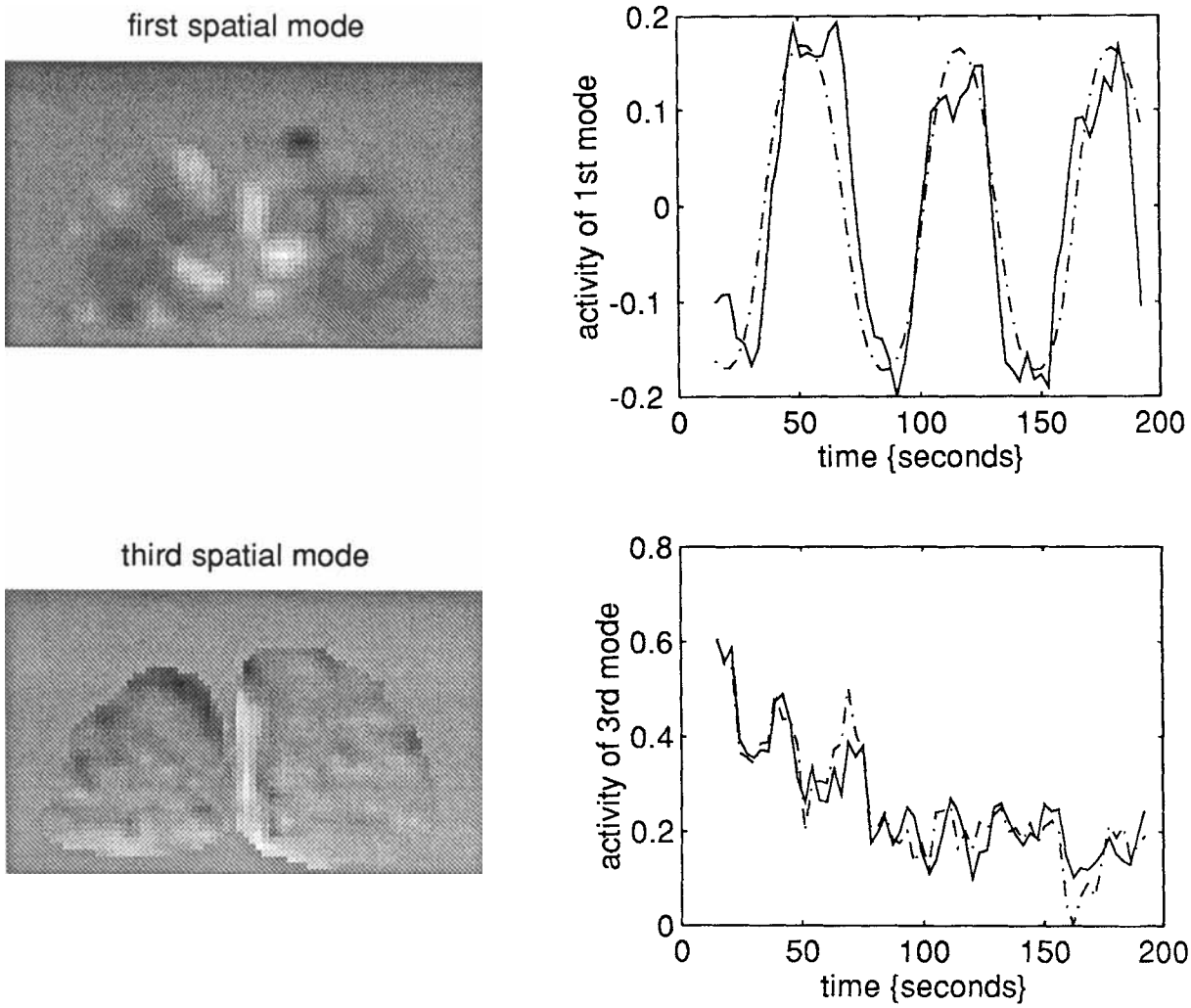

Figure 3.

SVD analysis of the fMRI time series referred to in the previous figure. **Left:** first (top) and third (lower) spatial modes or eigenimages following SVD. The greyscale is arbitrary and the images have been normalized to their maximum. **Right:** Time-dependent expression of the spatial modes. Right top: The periodic expression of the first mode due to photic stimulation (solid line) and that predicted by convolving the stimulation waveform with the hemodynamic response function, assuming a delay and dispersion of seven seconds (broken line). See Friston et al. [1994] for a full exposition. Right lower: Time-dependent expression of the third spatial mode due to movement artefact (solid line). The broken line corresponds to estimated diagonal movement using the data in the previous figure (Fig. 3).

1991a] both require mapping into some standard space (the generally accepted international standard is the space described in the atlas of Talairach and Tournoux [1988] as proposed by Fox et al. [1988]). Friston et al. [1991b] suggested that this mapping can be effected by "matching" an individual's image with an ideal reference image, model, or template, where the template conforms to the standard space in question. Clearly there are many other examples that could have been chosen for this section, but the one presented here is of immediate relevance for those engaged in functional mapping. This section also introduces two important extensions of the least squares approach which involve 1) a repeated or iterative application [where the spatially transformed object image $\Omega(q(x))$ is used recursively as a new object image $\Omega(x)$] and 2) making two sets of images from the original image pair and simultaneously solving for the spatial transformation that conjointly maps one set of images onto the other set.

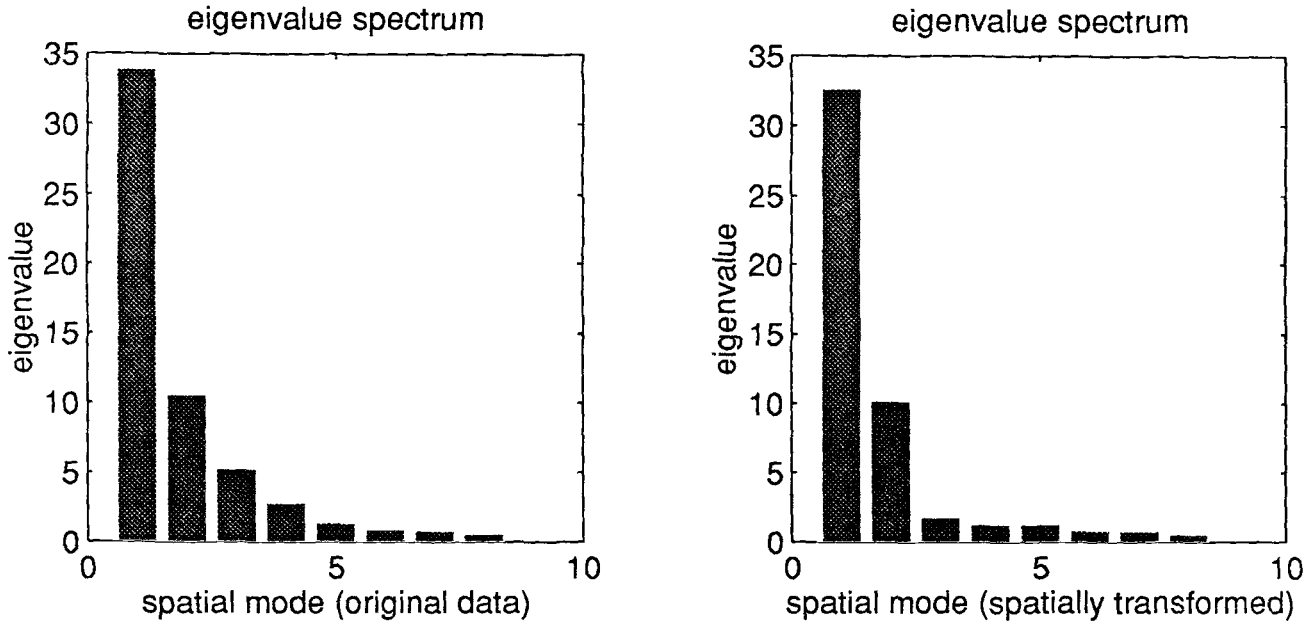

Figure 4.
Singular (squared) or eigenvalue spectrums following an SVD analysis of the fMRI time series before (**left**) and after (**right**) spatial transformation (realignment). The key difference is a decrease in the amount of variance attributable to the third spatial mode. This can be interpreted as a removal of movement artifacts.

PET to PET spatial normalization

The problem in this section is more general than in the previous section because the allowable transformations are not precisely specified and $\gamma_x(.)$, the functional component of the operator $f_x\{.\}$, is not known. This case is, however, not as general as situations considered later: We know that the resolution of the image process to be matched is the same (i.e., $\mathbf{c} = \mathbf{I}$, the identity matrix) and consequently Equation (5) reduces to:

$$[\text{diag}(\dagger).\boldsymbol{\beta}^f - \text{diag}(\partial\Omega/\partial\mathbf{x}).\boldsymbol{\beta}^q].[\mathbf{u}_1\ \mathbf{q}]^T \approx \Omega \qquad (7)$$

assuming a first order approximation for $\gamma_x(.)$. This first order approximation can be justified given that the images are of the same modality. Notice also that the zeroth order term (the constant) has been omitted, since we expect zero counts in one image to correspond to zero counts in the other. The basis functions ($\boldsymbol{\beta}^f$ and $\boldsymbol{\beta}^q$) can be arbitrary as long as they are smooth. In the present (and subsequent) example the basis functions for both $\mathbf{u}_1$ and $\mathbf{q}$ were the same and are shown in Figure 5. These basis functions correspond to Fourier modes, obtained by incrementing the spatial frequencies by $\pi/2$ and orthogonalising the resulting basis set. These basis functions can be quite arbitrary as long as they are smooth and cover the "space" of distortions in a reasonably comprehensive way. The exact nature and number of basis functions would probably vary from application to application. For simplicity we use the same set here throughout.

Spatial normalization

The object image $\Omega(x)$ was taken from the SPM (MRC Cyclotron Unit, London, and see Friston et al. [1991b]) library of template images and corresponds to a transverse section lying 12 mm above the intercommissural plane. The reference image $\dagger(x)$ was the corresponding slice from a normal subject acquired as described above. Although we present a spatial normalization of a single slice, it should be noted that this normalization is generally applied in three dimensions.

In this example we have used the "template" image as the object image (the image subject to spatial transformation). The designation of which image is the object and which the reference is usually arbitrary: The spatial transformation from object to reference is given by:

$$q(x) \equiv \mathbf{x} + \boldsymbol{\beta}^q.\mathbf{q}$$

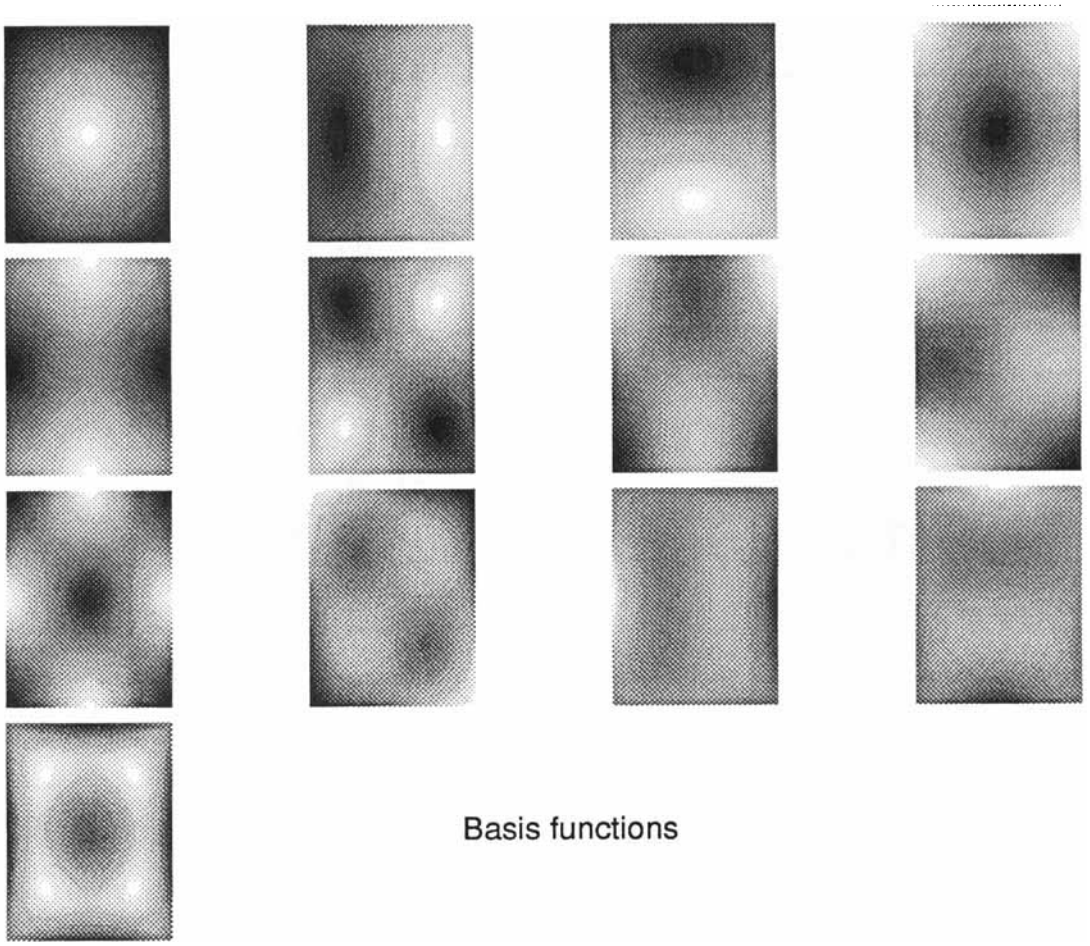

Figure 5.
The basis functions used in subsequent nonlinear spatial transformations and intensity transformation expansions. The gray scales are arbitrary and each function has been normalized to its maximum.

where $q(x)^{-1}$ is the complementary or inverse transformation from reference to object:

$$q(x)^{-1} \equiv \mathbf{x} - \mathrm{diag}(\mathbf{I} + \partial\boldsymbol{\beta}/\partial\mathbf{x}.\mathbf{q})^{-1}\boldsymbol{\beta}^{q}.\mathbf{q}. \quad (8)$$

This approximate equality is easy to derive using a first order Taylor expansion. The spatial and voxel value transformations were computed according to Equation (7) and the spatial transformations applied to $\Omega(x)$. The result [i.e., $\Omega(q(x))$] was substituted for $\Omega(x)$ in Equation (7) and the second spatial transformation added to the first. This process was repeated 3 times (see below). The results of this analysis are presented in Figure 6. Figure 6 shows the individual's transverse image (reference, top right) and the template PET image (object, top left). Figure 6 (lower left) shows the object image following spatial transformation. The spatial congruency between the resampled image and the reference image is seen and is largely a result of a counterclockwise rotation (particularly of subcortical structures). The image on the lower right is also a spatially transformed object image, but the solution for the resampling was computed in a different way, as described next.

Comparison with nonlinear minimization

The iterative solution of Equation (7) can be evaluated in relation to nonlinear minimization (e.g., the Levenberg-Marquardt technique [More, 1977]) by examining the trajectory of the paths taken in the recursive least squares approach and that taken by a nonlinear search in the space of the spatial transformation coefficients **q**. The nonlinear minimisation solution was obtained by minimizing the square of the 2-norm (over voxel locations x):

$$\| t(x) \Sigma u_{1j}\beta_j^f(x) - \Omega(x + \Sigma q_k\beta_k^q(x)) \|^2 \quad (9)$$

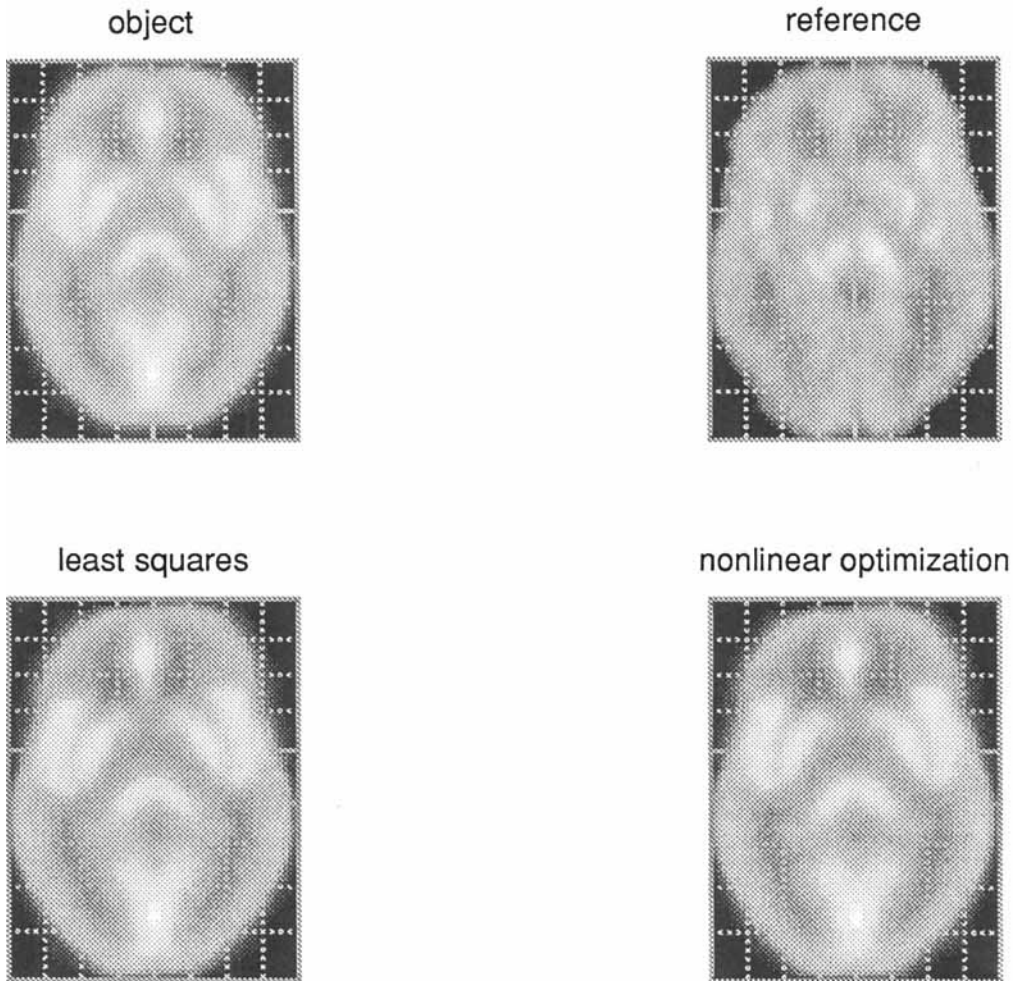

Figure 6.

Spatial normalization of PET images effected by spatial normalization of one PET image to another. The object image (**upper left**) is presented after spatial normalization (**lower left**) and shows a greater degree of correspondence with the reference image (**upper right**). The equivalent spatial transformation of the object image estimated using nonlinear minimization is shown on the **lower right.** All images have been scaled to their image maximum and are displayed on the proportional grid used by the atlas of Talairach and Tournoux [1988].

as a function of $[u_{11} \cdots\cdots u_{1j}\ q_1 \cdots\cdots q_j] \equiv [\mathbf{u}_1\ \mathbf{q}]$ using standard nonlinear minimization (as implemented in MATLAB, MathWorks Inc., Sherborn MA, USA). This solution is equivalent to solving Equation (7) but without the first order approximation implicit in Equation (3). The solutions for **q** were recorded at each iteration. The trajectory of these estimates was then compared with the trajectory traced out by the four recursive least squares solutions of Equation (7). These two trajectories were plotted in the two-dimensional subspace of the search space associated with the largest singular values. This is simply a device to view the trajectories from a direction that reveals the greatest excursions.

Despite the fact that the spatially transformed images in Figure 6 (lower panels) look very similar, the solutions obtained by least squares and nonlinear minimization were different. The results of this trajectory analysis are presented below and illustrate two key points: 1) the least squares approach found the global minimum whereas the nonlinear minimization did not, and 2) the search strategies differ fundamentally in their nature.

Figure 7 (top left and right) shows the singular distortions (c.f. principal warps [Bookstein, 1989]) or spatial transformations associated with the largest two singular values following SVD of the sequence of solutions for **q** (using both the least squares and

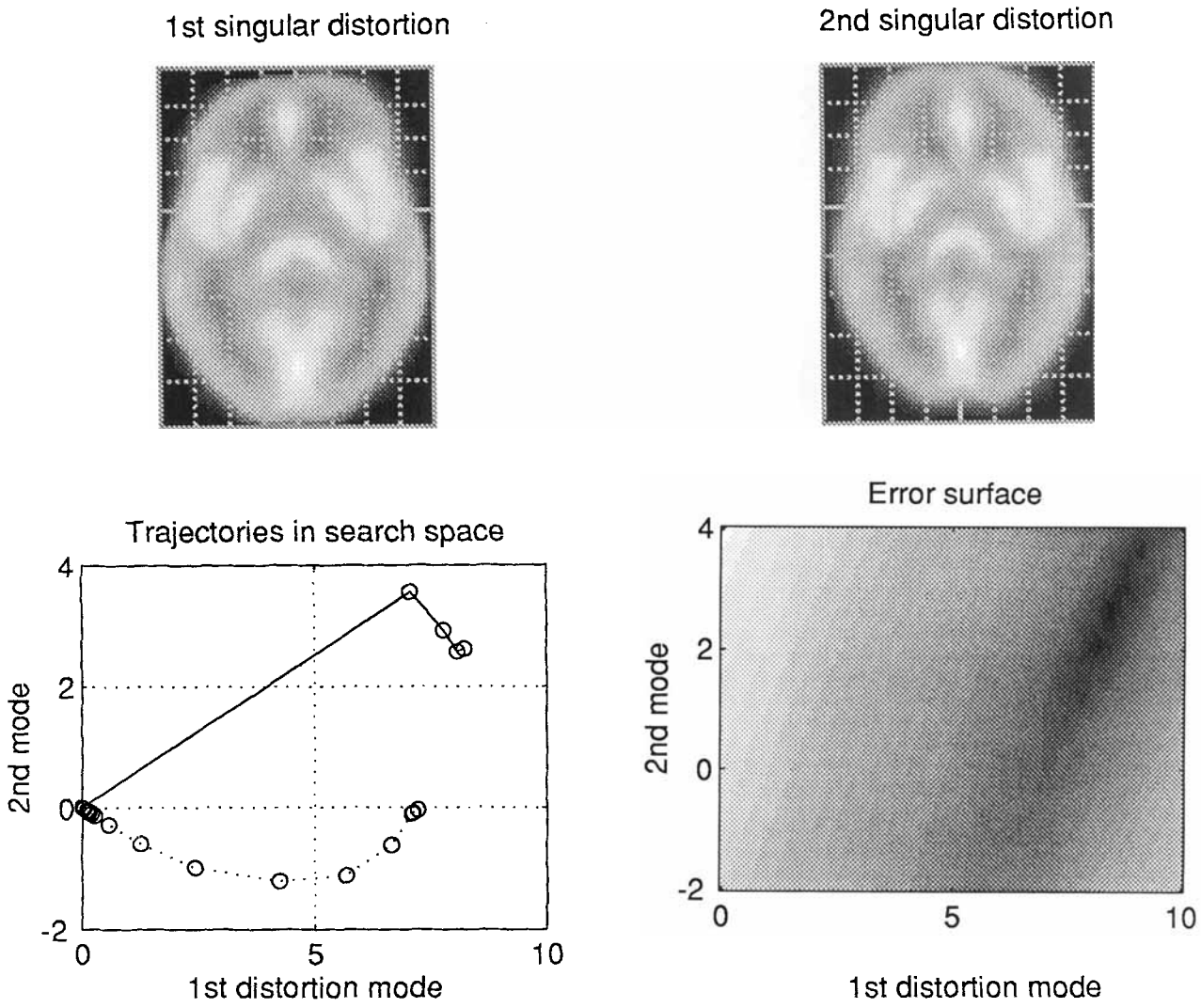

Figure 7.

Comparison of the least squares approach and nonlinear minimization in terms of searches over an error surface. **Upper left** and **upper right:** Singular warps or distortions defined by an SVD of the search trajectories in the space of the basis functions. These two singular warps correspond to the axes in the lower panels. The two warps accounted for the greatest excursions of the search trajectories and are orthogonal. Each singular warp has been applied to the object image (Fig. 6, top left). **Lower left:** Search trajectory in the space defined by the singular warps. Solid line, least squares; broken line, nonlinear minimization. **Lower right:** The corresponding error surface computed as a two-dimensional subspace of the search space. This subspace includes the final solution of the nonlinear minimization algorithm.

nonlinear minimization). These distortions are simply a linear combination of the basis functions. This linear sum is determined by the singular vectors associated with the largest singular values. The two distortional modes (Fig. 7, top left and right) correspond to the vertical and horizontal dimensions of the search subspace shown in Figure 7 (lower left panel). The corresponding error surface is depicted in the lower right panel. This surface reflects how "far off" the match is, in terms of the two singular distortions. The error surface was computed by varying the first two singular distortions, whilst using the final nonlinear estimate for the other parameters (remaining singular distortions and $\mathbf{u}_1$) using Equation (9). It is immediately obvious that the two trajectories (least squares—solid and nonlinear minimization—broken) converge to the different solutions. The nonlinear minimization found a local minimum. Furthermore, the recursive least squares approach used a handful of steps whereas the nonlinear minimization took over 20 iterations to

converge. The number of floating point operations (flops) per iteration taken by the nonlinear minimization was 2.7 times the number of flops required by one least squares solution. In short, the least squares approach will usually be an order of magnitude more efficient than an iterative nonlinear equivalent.

It is instructive to contrast the explicit least squares and nonlinear minimization. In anthropomorphic terms both approaches want to find the global minimum in a landscape defined by Equation (9) (the error surface in Fig. 7). The nonlinear minimization starts at an arbitrary location and, with acknowledged ignorance of all but the local landscape, sets of one step at a time always trying to chose the "best" path based on local features. The least squares approach is more pretentious and makes some (possibly) unwarranted assumptions about the global shape of the landscape (e.g., it assumes the landscape is parabolic) and, based on local features, goes straight to the (anticipated) lowest point. However, because the landscape is not quite as "well behaved" as the least squares thinks, it may need to "home in" on the global minimum, hence the iterative approach adopted in this section.

MRI to MRI

The last part of this section deals with a simple extension to the least squares approach. Here we deal with MRI to MRI matching and assume, as in the previous section, that $\mathbf{c} = \mathbf{I}$ and $\gamma_x\{.\}$ has only a first order term. In fact, in this application we assume $f_x\{y\} = y$. Now consider some arbitrary function $\gamma_i\{.\}$ applied to both $\dagger(x)$ and $\Omega(x)$ where $\gamma_i\{\dagger(x)\} = \dagger_i(x) \equiv \dagger_i$ and $\gamma_i\{\Omega(x)\} = \Omega_i(x) \equiv \Omega_i$. Equation (7) can be generalized to:

$$[\mathrm{diag}(\dagger_i).\boldsymbol{\beta}^f - \mathrm{diag}(\partial\Omega_i/\partial\mathbf{x}).\boldsymbol{\beta}^q].[\mathbf{u}_1\ \mathbf{q}]^T \approx \Omega_i.$$

Because we assume $f_x\{y\} = y$, this simplifies to:

$$\dagger_i - \mathrm{diag}(\partial\Omega_i/\partial\mathbf{x}).\boldsymbol{\beta}^q.\mathbf{q}^T \approx \Omega_i.$$

Because the spatial transformations are the same irrespective of the intensity transformations $\boldsymbol{\gamma}_i\{.\}$ we can solve for $\mathbf{q}$ simultaneously using several $\boldsymbol{\gamma}_i\{.\}$ functions:

$$\begin{aligned} \dagger_1 - \mathrm{diag}(\partial\Omega_1/\partial\mathbf{x}).\boldsymbol{\beta}^q.[\mathbf{u}_1\ \mathbf{q}]^T \quad & \Omega_1 \\ \dagger_2 - \mathrm{diag}(\partial\Omega_2/\partial\mathbf{x}).\boldsymbol{\beta}^q \quad \approx & \ \Omega_2 \\ \dagger_3 - \mathrm{diag}(\partial\Omega_3/\partial\mathbf{x}).\boldsymbol{\beta}^q \quad & \Omega_3 \end{aligned} \qquad (10)$$

and so on. In simple terms this extension means that we can extract any feature from both the reference and object image and match the resulting images. Because the spatial transformation is the same for all possible features we can combine several feature-specific image pairs to estimate the best spatial transformation. This extension depends on the fact that the $f_x\{.\}$ has a simple form. A more general extension of this sort is presented in the discussion.

The following example is meant to illustrate this idea more clearly. In matching two homologous structural (T1-weighted) MRI images from different subjects, one might simply use Equation (7) and proceed in an analogous way to the PET–PET normalization in the previous section. However, in so doing one would be implicitly matching white matter to white matter (because in T1-weighted images white/nonwhite boundaries dominate). A useful extension would be to segment the images into gray matter and white matter and match gray matter to gray matter and white to white. This can be effected simultaneously with Equation (10) and is simply implemented by chosing $\gamma_i\{.\}$ to perform a (crude) segmentation. In the present example we used:

$$\gamma_i\{\Omega(x)\} = c(x) * \exp(-(\Omega(x) - v_i)^2/2\sigma^2) \qquad (11)$$

where v_1 corresponds to the average gray matter intensity levels (0.52 of the image maximum) and v_2 corresponds to white matter levels (0.86 of the image maximum). σ controls the width of the "segmentation window" (we used 0.3). c(x) was a convolution kernel of full width at half maximum (FWHM) 4 voxels to ensure that smoothness constraints were met. Note that this "segmentation" is not very rigourous but is sufficiently good for the current purposes.

The results of this analysis are shown in Figure 8. The object image (that to be spatially transformed) is seen in the upper left panel and the reference image is seen in the upper right panel. The lower panels show the transformed object image (lower left) and the same superimposed on the reference image (lower right panel). The reshaping of the object image is particularly pronounced in the bottom right (occipital) region (Fig. 8, lower left). The two segmentation functions were applied to both the spatially normalized object image and the reference MRI images (omitting the convolution) to reveal the conjoint spatial matching of gray matter (Fig. 9, upper panels—transformed object and reference images) and white matter (lower panels). Generalization to three dimensions is only a question of computer resources; however, the resources required to manipulate volumetric high resolution MRI data should not be underestimated.

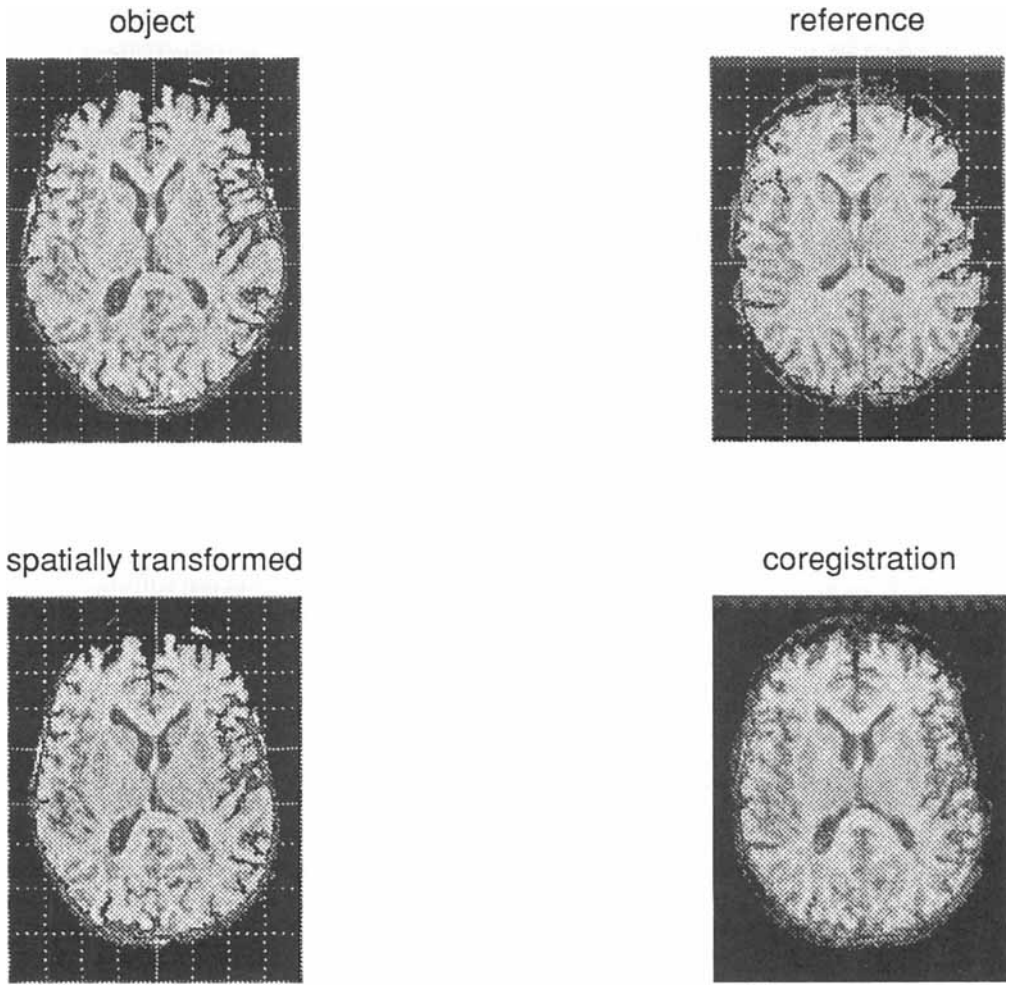

Figure 8.
Matching MRI to MRI. The object images before (**upper left**) and after (**lower left**) spatial transformation. The reference image that has been spatially approximated (**upper right**). The spatially transformed object and reference images have been superimposed to illustrate the coregistration (**lower right**). All images have been scaled to their maximum.

Between modality, within subjects

This section is concerned with the problem of cross-modality registration. The importance of this problem lies in relating anatomy to functional organization in the brain. Structure–function relationships are being elucidated with increasing precision by mapping data from functional time-series onto an individual's high resolution MRI image. The problem considered here is to match a PET image to a transverse high resolution MRI scan obtained from the same subject. This problem, once solved (in three dimensions), uniquely specifies the orthogonal transformation which brings the MRI and PET data into alignment.

In this section we concentrate more on the intensity transformation (the expansion of $f_x\{.\}$). In previous sections this expansion was trivial because the images were acquired with the same modality and a simple relationship could be assumed. In this section there is no simple relationship between MRI and PET voxel values even if the images were congruent. Indeed, not only is this relationship highly nonlinear, it is also likely to be highly nonmonotonic and nonstationary. There are many forms that the expansion of $f_x\{.\}$ could take. We present here an expansion designed specifically for the current application and which uses the same linearizing device (Taylor's theorem and a first order approximation) as for the spatial transformation.

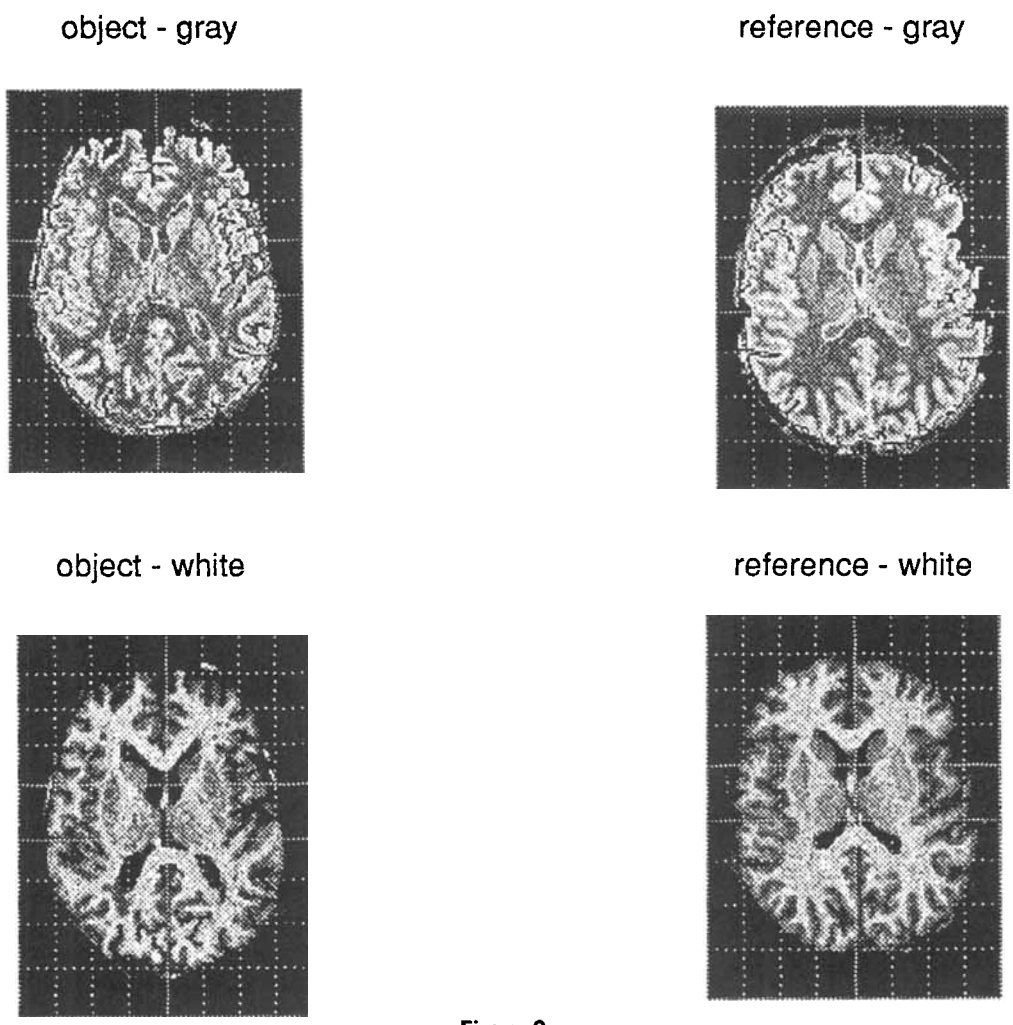

Figure 9.
The efficacy of the spatial transformation in terms of the (crudely) segmented MRI images. Grey matter segmented images following spatial normalization of the object image (**upper left**) and the reference image (**upper right**). **Lower left and right:** Equivalent images segmented for white matter. All images have been scaled to their maximum.

If one accepts the conjecture that the source of the PET signal is predominantly from gray matter, then the intensity transformation that maps an MRI image $\dagger(x)$ onto a PET image $\Omega(q(x))$ would involve grey matter segmentation $s_x(\dagger(x),v(x))$, nonstationary scaling, and convolution into the resolution of the PET image. Mathematically one could express this as:

$$f_x\{\dagger(x)\} = c(x) * u_0(x).s_x(\dagger(x), v(x))$$

where

$$s_x(\dagger(x), v(x)) = \exp(-(\dagger(x) - \{v_g + v(x)\})^2/2\sigma^2) \quad (15)$$

where $c(x)$ is a convolution kernel, $u_0(x)$ is a nonstationary but smoothly varying scaling coefficient, σ is the "standard deviation" of the segmentation kernel, v_g is the fixed estimate of gray matter intensity, and $v(x)$ is the deviation from this estimate at a particular point in the brain x. Equation (12) is not in a form that permits a linear least squares solution for the unknowns $u_0(x)$ and $v(x)$. In order to make Equation (12) amenable to a least squares analysis, one can adopt the same approach used for the spatial transformation in Equation (3), namely, using a first order approximation of the Taylor series. In this case the derivatives are not with respect to spatial distortions but the derivative of the

segmentation function with respect to small deviations in the grey matter intensity $[\partial s(\dagger(x),0)/\partial v(x)]$.

$$\begin{aligned} f_x(\dagger(x)) &\approx c(x) * u_0(x).\{s(\dagger(x), 0) \\ &\quad + v(x).\partial s(\dagger(x), 0)/\partial v(x)\} \\ &\approx c(x) * \{u_0(x).s(\dagger(x), 0) \\ &\quad + u_1(x).\partial s(\dagger(x), 0)/\partial v(x)\}. \end{aligned}$$

As usual we can expand the nonstationary coefficients u_0 and u_1 in terms of basis functions $u_i(x) = \Sigma u_{ij}\beta_j^f(x)$, giving, in matrix notation:

$$f_x(\dagger(x)) \equiv [\mathbf{c}.\mathrm{diag}(\dagger).\boldsymbol{\beta}^f\ \mathbf{c}.\mathrm{diag}(\partial \mathbf{s}/\partial \mathbf{v}).\boldsymbol{\beta}^f].[\mathbf{u}_0\ \mathbf{u}_1]^T. \quad (13)$$

The important thing to note here is that the *form* of the "segmentation function" $f_x(\dagger(x))$ is the same everywhere but the actual function can vary from place to place. This is important because one cannot guarantee exactly the same relationship between MRI and PET voxel values in every part of the image (e.g., lesions, focal activations, and field heterogeneities will introduce nonstationariness into the relationship).

Because this section deals with within subject transformations the spatial component is a rigid body transformation with six parameters. The simultaneous solution for both intensity and spatial transformations is given by the solution of:

$$[\mathbf{c}.\mathrm{diag}(\dagger).\boldsymbol{\beta}^f\ \mathbf{c}.\mathrm{diag}(\partial \mathbf{s}/\partial \mathbf{v}).\boldsymbol{\beta}^f - \partial\Omega/\partial \mathbf{q}].[\mathbf{u}_0\ \mathbf{u}_1\ \mathbf{q}]^T \approx \Omega \quad (14)$$

for $\mathbf{u}_0\ \mathbf{u}_1$ and $\mathbf{q}$. $\partial\Omega/\partial\mathbf{q}$ was estimated directly as in the section on realignment of fMRI time series. Because the effective resolution of the MRI image is approximated by its voxel dimensions and that of the PET image was about 8 mm, we chose $\mathbf{c}$ to correspond to a two-dimensional convolution with a Gaussian filter with FWHM 8 mm. v_g was set at 0.52 of the MRI image maximum and σ was 0.3.

The results of this analysis, for roughly homologous slices, are presented in Figure 10, which shows the object image (best guess transverse slice from the PET volume—top left) and the reference image (an arbitrary slice from a volume MRI image of the same subject—top right). The lower image is the PET slice following spatial transformation. The congruence is demonstrated on the lower right where the spatially transformed PET image and the reference MRI image are superposed. In fact, the registration here was already quite good and the spatial normalisation involved only a small translation and rotation. Of greater interest is the solution for the MRI intensity transformation.

The intensity transformation

Here we consider the intensity transformation that is implicitly applied to the MRI image in Equation (14). Hitherto this component of the solution has not been very interesting, but in between modality applications the transformation can be considered of primary importance and the spatial component of secondary interest (see applications section in discussion). The intensity transformed MRI image that best matches (in a least squares sense) the spatially transformed PET image is given by Equation (13). This estimate is shown in Figure 11 (bottom left) and can be thought of as an MRI image emulating a PET image. The correspondence with the real PET image (above) is apparent and remarkably good considering we made the somewhat unreasonable assumption that all the PET signal came from grey matter.

The intensity transformed MRI image obtained before convolution [setting $\mathbf{c} = \mathbf{I}$ in Eq. (13)] is seen in Figure 11 on the right. This is the "best" distribution of functional activity that could explain the observed PET scan before convolution with the point spread function, where the distribution is constrained by structural information in the MRI image. Equivalently, this is a least squares solution for the distribution of functional activity based on the underlying anatomy. We expand on the potential importance of this "virtual modality" in the discussion.

The actual solution for $f_x\{.\}$ in Equation (13) clearly depends on position in the image. Two examples are given in Figure 12 according to the estimates obtained. The examples come from cortical and subcortical grey matter voxels indicated by black dots in the left lateral secondary sensory cortex and the left thalamus. The corresponding cortical (solid line) and subcortical (broken line) functionals $f_{cortical}\{.\}$ and $f_{subcortical}\{.\}$ are shown on the right of Figure 12. It is immediately obvious that the cortical grey matter activity is greater than the subcortical estimate. The fact that this relative difference is reversed in the PET image is due to partial voluming effects on signals from the cortical sheet. More importantly, the grey matter intensity values for the cortical MRI voxels were lower than for the subcortical voxels, i.e., the peak of $f_{cortical}\{.\}$ corresponds to a lower MRI voxel intensity than the $f_{subcortical}\{.\}$ peak.

In this section we have presented a simple (but still effective) example of PET to MRI matching. One could

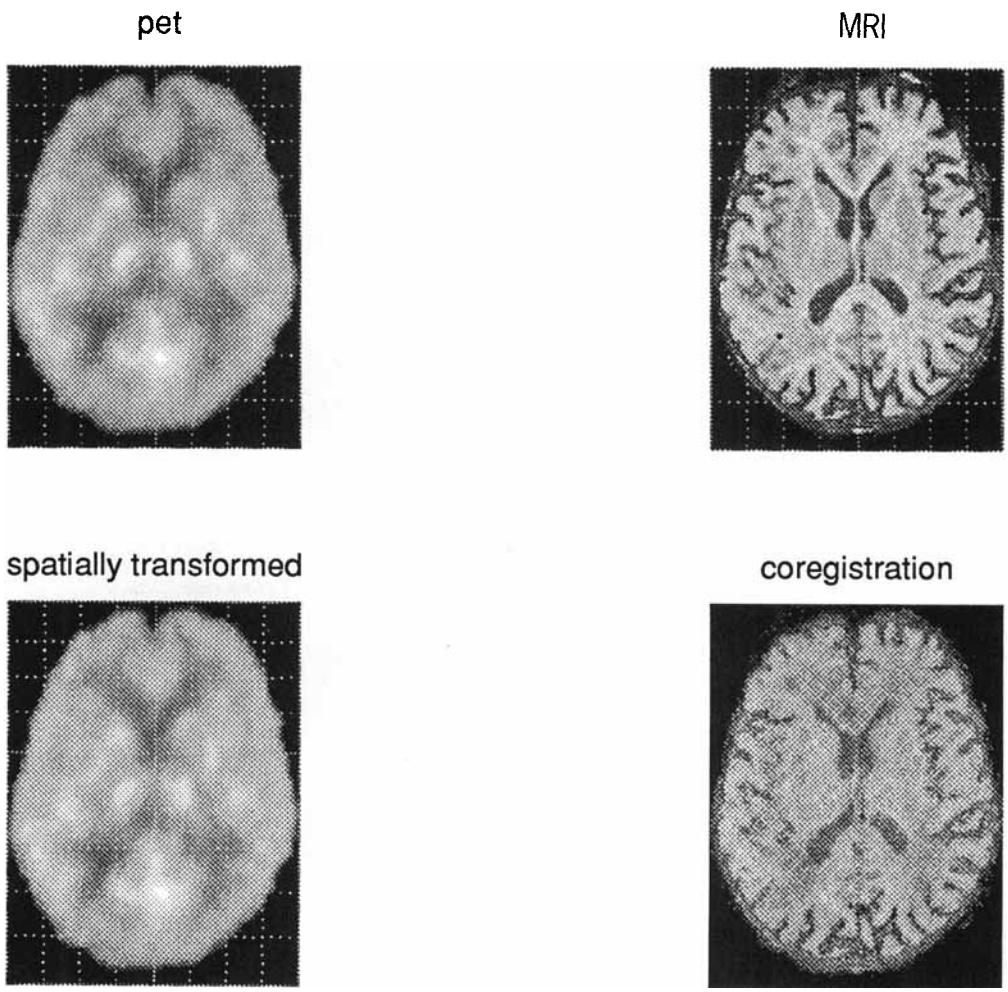

Figure 10.
Cross-modality spatial transformations. Transverse PET slices before (**upper left**) and after (**lower left**) spatial normalization to a reference MRI image (**upper right**). **Lower right:** The coregistration. All images have been scaled to their maximum.

easily generalize the approach to include white matter contributions or indeed make the form of the segmentation kernel more general using a greater number of parameters.

Between modality, between subjects

This final section is included for completeness. Here we match (†) a transverse MRI slice from the individual used in the previous sections and (Ω) the corresponding transverse section from the MRC library of PET templates used in the section on PET to PET normalization. This is the most general problem considered in this paper and requires a solution for the transformation coefficients with no simplifications. In this example we have deliberately degraded the MRI data by resampling to render voxel size the same as the PET data. Here the spatial transformation is not constrained to be affine and Equation (14) has to be generalized to

$$[\mathbf{c}.\mathrm{diag}(\dagger).\boldsymbol{\beta}^{f}\ \mathbf{c}.\mathrm{diag}(\partial \mathbf{s}/\partial \mathbf{v}).\boldsymbol{\beta}^{f} - \mathrm{diag}(\partial \Omega.\partial \mathbf{x}).\boldsymbol{\beta}^{q}].[\mathbf{u}_0\ \mathbf{u}_1\ \mathbf{q}]^{T} \approx \Omega. \quad (15)$$

The basis functions ($\boldsymbol{\beta}^{f}$ and $\boldsymbol{\beta}^{q}$) for intensity and spatial transformations were the same as in previous sections (Fig. 4). The expansion of $f_x(x)$ was in terms of a Gaussian segmentation kernel as in the previous section. $\mathbf{c}$ corresponded to a two-dimensional convolution with a Gaussian kernel of FWHM of 8 mm.

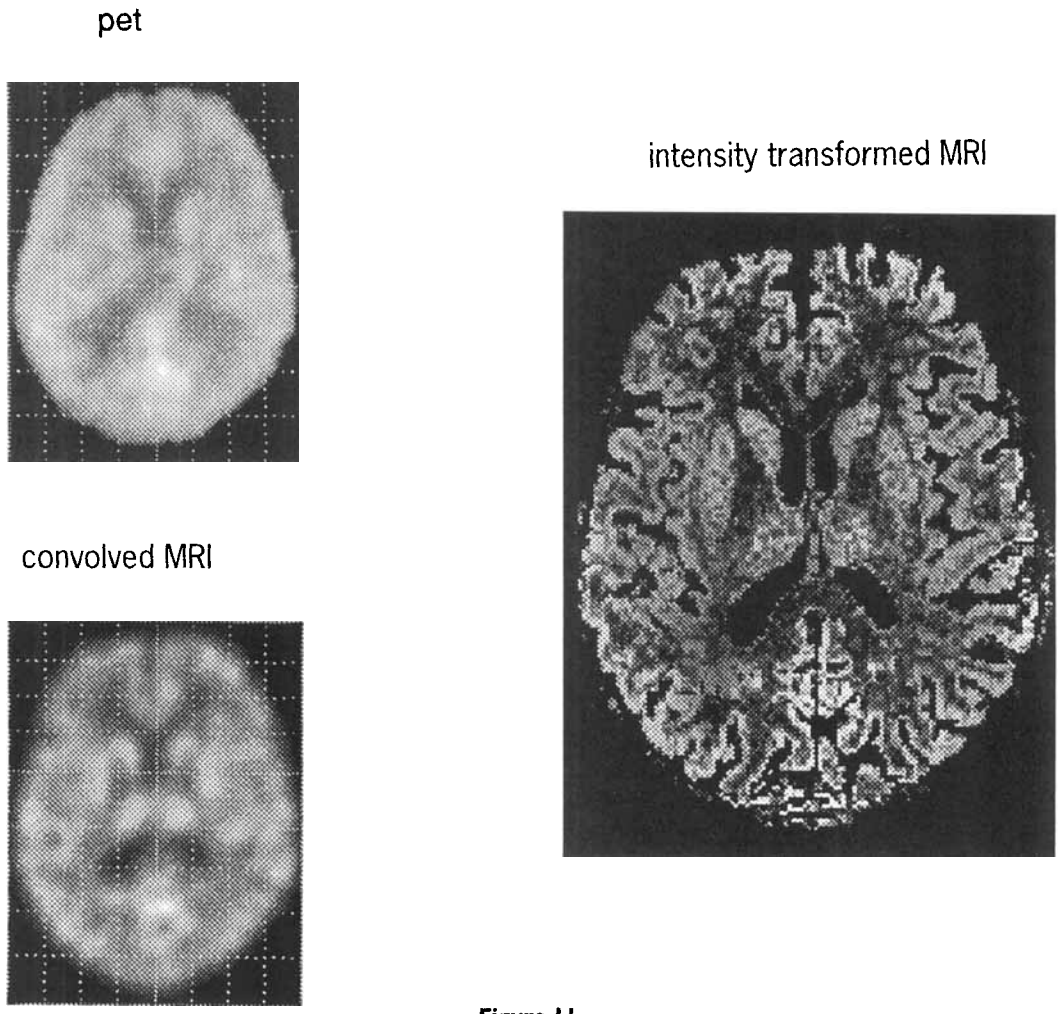

Figure 11.
Cross-modality intensity transformations. **Upper left:** Spatially transformed PET image (as in Fig. 10, lower left). **Right:** The intensity transformed MRI image without convolution. After convolution (**lower left**) this image approximates the PET image in a least squares sense. All images have been scaled to their maximum.

The results of this analysis are presented in Figures 13 and 14 using a similar format as in the previous section (Figs. 10, 11). The spatial congruence of the MRI image and transformed PET image and delimitation of gray matter in the MRI image are evident. The technique appears to be fairly resistant to the degradation of the MRI images.

DISCUSSION

This paper has presented a generic approach to the spatial transformation of image processes. The approach is automatic (is noninteractive), finds explicit solutions (is noniterative), and solves general problems (is nonlinear). The technique depends on partitioning the differences between an object image and a reference image into two components. The first component is due to differences that remain after discounting the effects of image misregistration or noncongruence. The second source of differences results from spatial translations, rotations, and distortions. Both types of difference are modeled with expansions in terms of basis functions, polynomials, and Taylor series using low order approximations in such a way as to render the problem linear. The requisite spatial and image transformations are then solved for in a least squares sense.

In this paper we have focused on the realignment of neuroimaging time-series, spatial normalization required for voxel-based analysis of activation studies,

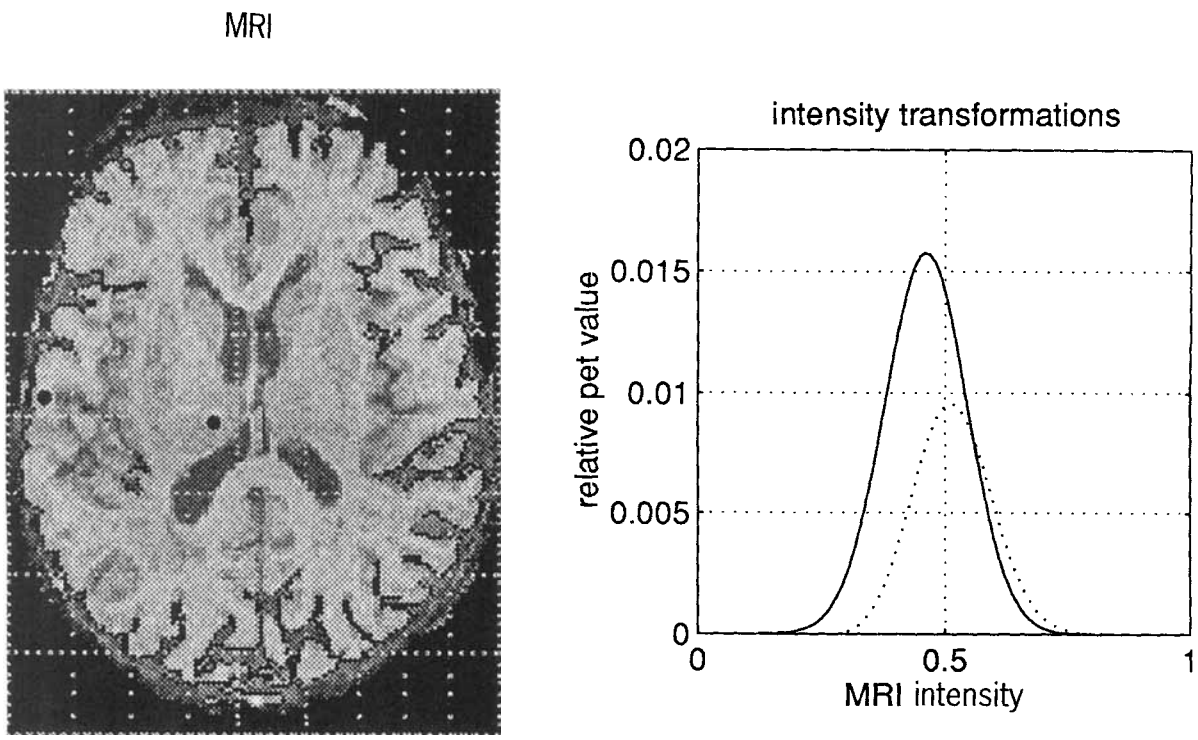

Figure 12.
The transformation functions for two gray matter voxels in the MRI image. **Left:** The position of the two voxels in cortical and subcortical regions (black dots). **Right:** The corresponding intensity transformation functions. Solid line, cortical voxel; broken line, subcortical voxel.

cross-modality registration, and spatial normalization of images from different modalities. The nature of the transformation is defined by the constraints under which the transformation is applied. These constraints are embodied in the operational equations described. The minimal constraints adopted in this work pertain to the preservation of local contiguities and the local stationariness of operators which map one modality into another. These constraints can be framed in terms of smoothness, namely, the spatial transformation represents a smooth mapping and the coefficients of any intensity transformation (functionals) change slowly with position. Smoothness is imposed by using smooth basis functions.

We have presented a series of ideas and techniques some of which are fundamental and some of which are not. We consider the following points to be important aspects of the approach:

1. Reliability takes precedence over validity. This requires a non-label-based approach that, in this instance, minimizes the sum of squares between two image processes.
2. The differences between two images can be attributed to 1) noncongruence and 2) differences extant when the images are in perfect register.
3. The transformations which minimize these differences (in a least square sense), namely the spatial transformation and intensity transformation, are solved for simultaneously.
4. Both transformations are defined in the space of some basis functions. The nature of the basis functions (e.g., smoothness) embodies the constraints under which the transformations are effected.
5. The minimal constraints on the basis functions relate to preservation of local contiguity relationships and the local stationariness of the intensity transformation. This is equivalent to using smooth basis functions.
6. The solution for the spatial and voxel value transformations can, if appropriate, be formulated in linear terms, permitting an explicit least squares solution. Taylor series and other expansions are particularly useful in this regard. If they are not appropriate, standard nonlinear minimization or gradient descent techniques can be used.

Although possibly nonoptimal, Fourier basis functions are efficient in that they do not require empirical

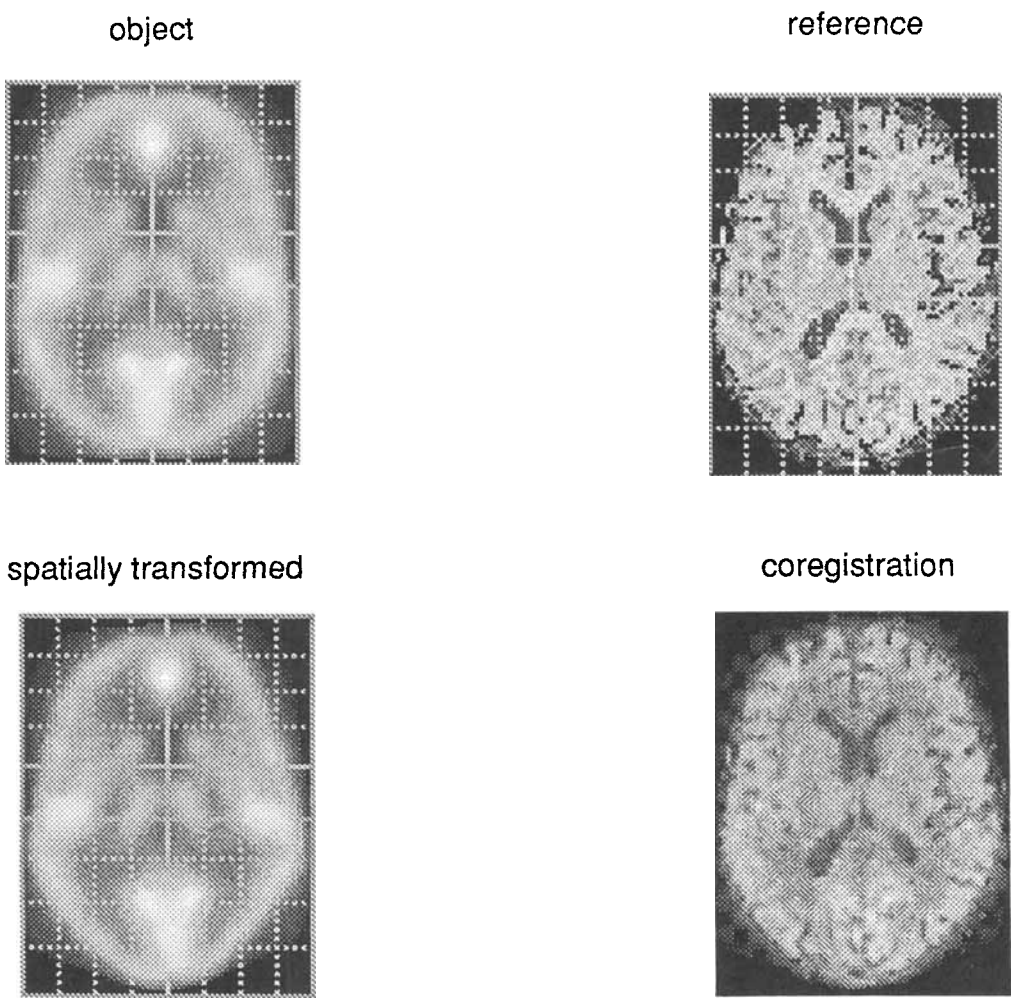

Figure 13.
As for Figure 10 but in this instance the PET and MRI images are subject to nonlinear spatial transformations because they did not derive from the same subject. All images have been scaled to their maximum.

characterization of the spatial autocovariance functions (c.f. the Karhunen Loeve expansion or SVD).

Applications

The applications of spatial and intensity transformations are numerous. We have demonstrated applications to the realignment problem and spatial normalisation. Here we consider other applications and extensions. Applications can be classified according to the goal of the transformation. The objectives of most transformations fall under three general headings: 1) reducing differences of a specific sort to facilitate comparison among images, 2) characterisation of differences in spatial topography, and 3) image restoration and segmentation.

The examples in this paper have focused on the first class of applications in the sense that image realignment and normalisation are usually implemented as a prelude to comparison among scans. The second class of applications asks "what are the important modes of anatomical (topographic) variation?" or "what are the anatomical differences between one set of scans and another?" The answers to both these questions depend on a complete specification of the spatial topography of each image. We propose that this specification could be in terms of the *spatial distortion required to map an arbitrary image onto some reference.* For example, the topography of an image can be characterized in terms of the coefficients corresponding to the spatial basis functions. This simple list of coefficients, taken in conjunction with the reference image, is a complete

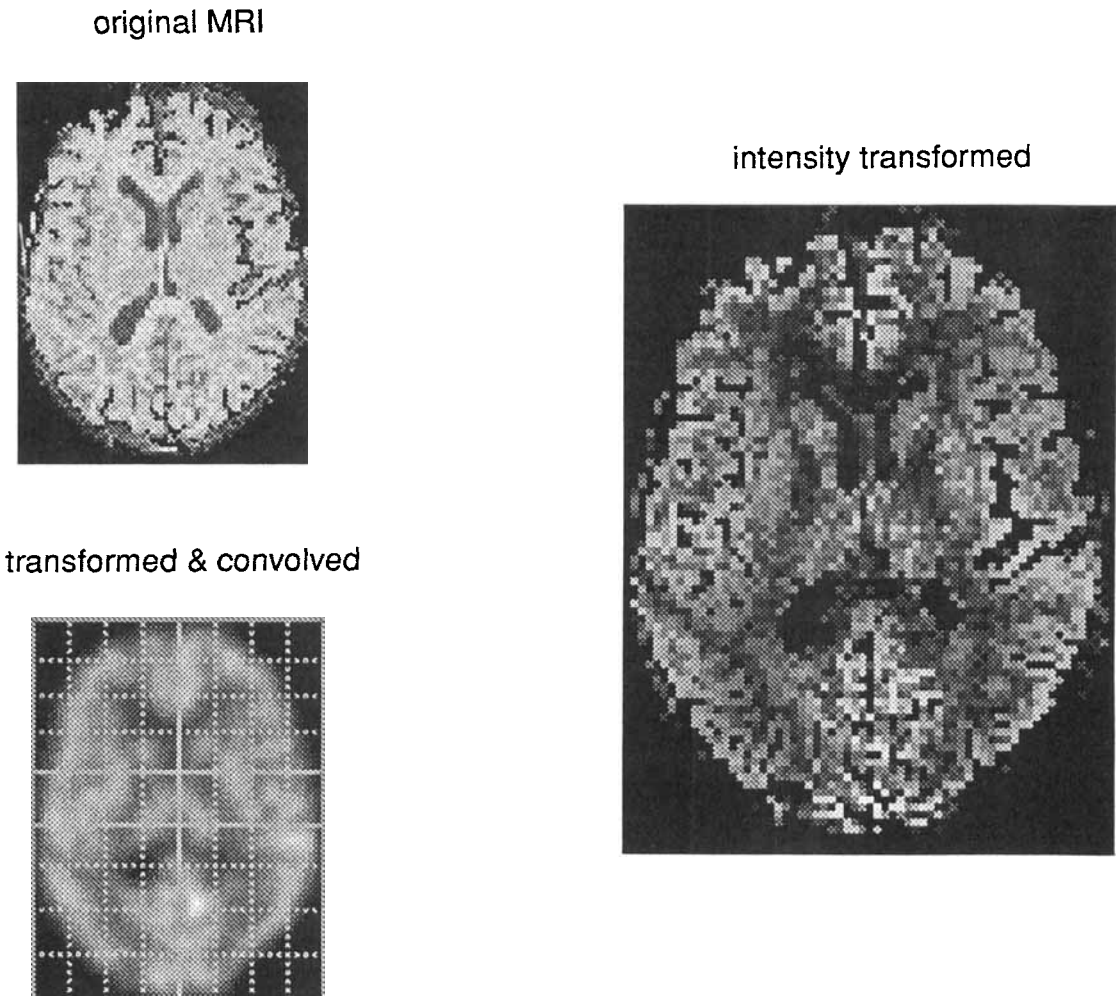

Figure 14.
As for Figure 11 but in this instance the PET and MRI images are subject to nonlinear spatial transformations because they did not derive from the same subject and the original MRI image is shown on the top left.

specification of the topography of the original image (down to the resolution imposed by the basis functions). The importance of this observation is that anatomical topography can be characterized by a multivariate measure (the coefficients) and is subject to conventional multivariate statistics.

Important examples of this characterization could include the normal modes of anatomical variability defined on a series of MRI scans from normal subjects. The exciting concept here is that once normal modes of anatomical variation are established *they can then be used as the basis functions in the transformations.* The charm of this "bootstrapping" is in constraining the transformations to lie in the space of normal anatomical variability. This would increase the face validity of the transformation and probably reduce the number of basis functions considerably. This is the subject of current work. Alternatively, important neurodevelopmental modes can be identified using MRI scans obtained during development (Nick Lange, personal communication). These modes are simply defined by SVD of the spatial transformations (or the coefficients of the spatial basis functions).

The third set of applications was referred to in the first section on PET–MRI matching. In this section we solved simultaneously for a spatial transformation and an intensity transformation that jointly matched a PET scan and an MRI scan from the same subject. The intensity transformation, considered in isolation, assigns functional (PET) values to structural objects in the MRI image. This transformation can be appreciated from two points of view: 1) it is a functional

categorization of anatomical structures of the sort implied by image segmentation, and alternatively, 2) the intensity transformed MRI image represents a least squares solution for the underlying flow distribution seen in the PET image. In this sense the transformed MRI image emulates a "restored" PET image, where the restoration embodies anatomical information (from the MRI). This second perspective suggests it may be possible to analyze single subject functional time-series (e.g., PET activation studies) using not the original functional data but the transformed MRI images. This multimodality application is currently being explored.

Extensions

There is a potentially important extension to the technique that we did not demonstrate. This extension involves solving for the spatial and intensity transformations simultaneously for the images and the images convolved with any number of convolution kernels. This is simply effected by stacking the matrices in Equation (5) on top of each other after premultiplying by the appropriate convolution matrix. For example, if we take an arbitrary convolution matrix § then from Equation (5)

$$\S.[c.\mathrm{diag}(f^0(\dagger)).\boldsymbol{\beta}^f\ c.\mathrm{diag}(f^1(\dagger)).\boldsymbol{\beta}^f \cdots -\mathrm{diag}(\partial\Omega/\partial x).\boldsymbol{\beta}^q].[\mathbf{u}_0\ \mathbf{u}_1 \cdots \mathbf{q}]^T \approx \S\,.\,\Omega$$

so for a series of convolution matrices $\S_i$:

$$\S_0.c.\mathrm{diag}(f^0(\dagger)).\boldsymbol{\beta}^f\ \S_0.c.\mathrm{diag}(f^1(\dagger)).\boldsymbol{\beta}^f \cdots -\S_0.\mathrm{diag}(\partial\Omega/\partial x).\boldsymbol{\beta}^q.[\mathbf{u}_0\ \mathbf{u}_1 \cdots \mathbf{q}]^T \approx \S_0.\Omega$$

$$\S_1.c.\mathrm{diag}(f^0(\dagger)).\boldsymbol{\beta}^f\ \S_1.c.\mathrm{diag}(f^1(\dagger)).\boldsymbol{\beta}^f \cdots -\S_1.\mathrm{diag}(\partial\Omega/\partial x).\boldsymbol{\beta}^q \approx \S_1.\Omega$$

$$\S_2.c.\mathrm{diag}(f^0(\dagger)).\boldsymbol{\beta}^f\ \S_2.c.\mathrm{diag}(f^1(\dagger)).\boldsymbol{\beta}^f \cdots -\S_2.\mathrm{diag}(\partial\Omega/\partial x).\boldsymbol{\beta}^q \approx \S_2.\Omega \qquad (16)$$

and so on.

For example, $\S_0$ could represent the identify matrix and $\S_1$ a differential operator. In this case the transformation solutions would simultaneously approximate the original images (Ω and †) and their first derivatives ($\mathbf{d\Omega/dx}$ and $\mathbf{d\dagger/dx}$). The constraints on $\S_i$ are that it should not make the first order approximation of the effect of spatial transformations unreasonable. This means the result of convolving Ω should still be smooth.

Limitations

The limitations of the technique described here relate to the "reasonableness" of the first order approximation in Equation (3) and any other constraints imposed by expanding in terms of basis functions, Taylor series, or polynomials. The first order approximation [Eq. (3)] is only a good one when the spatial distortions are small relative to smoothness. In a sense this is not a fundamental limitation because 1) the images can always be made sufficiently smooth using the formalism of the previous section [Eq. (16)], or 2) spatial differences can be successively reduced using the linear piece-wise approximation to a nonlinear search, as implemented in the recursive application (see above). Because the initial mismatch between object and reference should be small (relative to smoothness), whenever two images are matched the image with the poorer spatial resolution can be considered as Ω. Clearly one should start with the "best guess" registration.

Missing data appears to be handled in a reasonably graceful fashion as long as the least squares solution is restricted to voxels at which data exists for both image processes. This is no problem in image registration because the affine transformations specified for one part of the image exactly specify the transformations everywhere. For nonlinear transformations if one part of the image is missing no solution can be obtained for the homologous part of the other image. In this sense it is advisable to ensure that the reference image is more "complete" than the object image.

One potentially important limitation of smooth basis functions is that they are not always necessarily appropriate. For example, at the apposition of the cortices in the interhemispheric fissure there is spatial proximity but contiguity across the falx cerebri is a biological impossibility. In this instance basis functions that are smooth over the midsagittal plane may not be appropriate. In practice we have never found this to be a problem at the resolutions with which we commonly work. If it were a problem then the basis functions could be redesigned, or, equivalently, each hemisphere could be normalized separately.

One practical limitation is the amount of working memory available to compute the least squares solution. This can severely compromise the volume of data that can be dealt with and the number of basis functions (or the order of other expansions) that can be used. It should be noted that the actual software implementation does not adhere to the matrix equations above. For example, one would never actually construct diag(†) but would emulate the required matrix operation with the equivalent element by element operations (unless one had a software environment that could handle sparse matrices). In dealing with nonlinear spatial normalization of large volume data sets we have found the following strategy useful:

1) three-dimensional affine and nonlinear transformations based on sparse sampling (i.e., subsampling) followed by 2) two-dimensional or piece-wise (e.g., slice) nonlinear deformations with complete sampling.

Issues of validity

The criteria for "good" spatial transformations can be framed in terms of validity, reliability, and computational efficiency. The validity of a particular transformation device is not easy to define or measure and indeed varies with the application. For example, an orthogonal transformation may be perfectly valid for realignment but not for spatial normalization of an arbitrary brain into a standard stereotactic space. In general, the sorts of validity that are important in spatial transformations can be divided into 1) *face validity,* established by demonstrating the transformation does what it is supposed to, and 2) *construct validity,* assessed by comparison with other techniques or constructs. In functional mapping face validity is a complex issue. At first glance face validity might be equated with the coregistration of anatomical homologues in two images. This would be complete and appropriate if the biological question referred to structural differences or modes of variation. In other circumstances, however, this definition of face validity is not appropriate. For example, the purpose of spatial normalization (either within or between subjects) in functional mapping studies is to maximize the sensitivity to neurophysiological change elicited by experimental manipulation of sensorimotor or cognitive state. In this case the better definition of a valid normalization is that which maximizes condition-dependent effects with respect to error (and, if relevant, intersubject) effects. This will probably be effected when functional anatomy is congruent. This may or may not be the same as registering structural anatomy.

In the present work we have addressed validity at a number of levels. In the first section we established face validity with respect to known simulated movement and construct validity with respect to another approach [Woods et al., 1992]. Another aspect of face validity was addressed by showing that the algorithm removed a component from the functional variance that could be attributed to movement artifact. In the second section we examined construct validity in terms of standard nonlinear minimization and trajectories on an error surface.

Finally, with reference to the construction of "virtual modalities" using intensity transformations, we emphasise that the validity of this "modality" depends on the validity of the forms of the relationship, between voxel values in both modalities, that are assumed in the least squares solution.

In conclusion, we hope to have presented a reasonable solution to a fairly simple problem: how to match one image to another reliably, quickly, automatically, and with some degree of validity.

Note

Many of the algorithms presented in this paper have been implemented in MATLAB (MathWorks Inc., Sherborn, MA, USA) as part of the SPM (Statistical Parametric Mapping) package. The spatial normalisation component developed for PET uses a 12-parameter affine–six-parameter nonlinear transformation in three dimensions to match an individual's image to a library template. Our ASCII files (which are interpreted by MATLAB) are available from the authors.

ACKNOWLEDGMENTS

We thank Paul Fletcher, Robert Turner, and Peter Jezzard for contributing some of the images used above. We also thank John Mazziotta, Alan Evans, Peter Fox, Nick Lange, and Fred Bookstein for very useful discussions on the issues addressed in this paper and all our colleagues for their help and support in the development of these ideas.

REFERENCES

Alpert NM, Bradshaw JF, Kennedy D, Coreia JA (1990): The principal axis transformation—a method for image registration. J Nucl Med 31:1717–1722.

Amit Y, Grenander U, Piccioni M (1991): Structural image restoration through deformable templates. J Am Stat Assoc 86:376–387.

Bookstein FL (1989): Principal warps: Thin plate splines and the decomposition of deformations. IEEE Trans Pattern Anal Mach Intell PAMI11:567–585.

Collins DL, Neelin P, Peters TM, Evans AC (1994): Automatic 3D intersubject registration of MR volumetric data in standardized Talairach space. J Comput Assist Tomogr 18:192–205.

Fox PT, Mintun MA, Reiman EM, Raichle ME (1988): Enhanced detection of focal brain responses using intersubject averaging and change distribution analysis of subtracted PET images. J Cereb Blood Flow Metab 8:642–653.

Fox PT, Mintun MA (1989): Non-invasive functional brain mapping by change distribution analysis of averaged PET images of $H^{15}O_2$ tissue activity. J Nucl Med 30:141–149.

Friston KJ, Frith CD, Liddle PF, Frackowiak RSJ (1991a): Comparing functional (PET) images: The assessment of significant change. J Cereb Blood Flow Metab 11:690–699.

Friston KJ, Frith CD, Liddle PF, Frackowiak RSJ (1991b): Plastic transformation of PET images. J Comput Assist Tomogr 15:634–639.

Friston KJ, Jezzard P, Turner R (1994): Analysis of functional MRI time-series. Hum Brain Mapping 2:69–78.

Kosugi Y, Sase M, Kuwatani H, Kinoshita N, Momose T, Nishikawa J, Watanabe T (1993): Neural network mapping for nonlinear

stereotactic normalization of brain MR images. J Comput Assist Tomogr 17:455–460.
Lange N (1994): Some computational and statistical tools for paired comparisons of digital images. Stat Methods Medial Res 3:23–40.
More JJ (1977): The Levenberg-Marquardt Algorithm: Implementation and theory. In: Watson GA (ed): Numerical Analysis. Lecture Notes in Mathematics 630. New York: Springer-Verlag, pp 105–116.
Pelizzari CA, Chen GTY, Spelbring DR, Weichselbaum RR, Chen CT (1988): Accurate three-dimensional registration of CT, PET and MR images of the brain. J Comput Assist Tomogr 13:20–26.
Spinks TJ, Jones T, Bailey DL, Townsend DW, Grootnook S, Bloomfield PM, Gilardi MC, Casey ME, Sipe B, Reed J (1992): Physical performance of a positron tomograph for brain imaging with retractable septa. Phys Med Biol 37:1637–1655.
Steinmetz H, Seitz RJ (1991): Functional anatomy of language processing: Neuroimaging and the problem of individual variability. Neuropsychologia 29:1149–1160.
Talairach J, Tournoux P (1988): Co-Planar Stereotaxic Atlas of the Human Brain Stuttgart: Thieme.
Woods RP, Cherry SR, Mazziotta JC (1992): Rapid automated algorithm for aligning and reslicing PET images. J Comput Assist Tomogr 16:620–633.

APPENDIX

This appendix contains nothing new for the general reader. It is included for those who wish to verify the derivations in detail and/or implement the matrix equations in an application.

Consider the general problem of spatially transforming one image so that it matches another. The differences between the object image $\Omega(x)$ and the reference image $\dagger(x)$ can be attributed to 1) differences in intensity (given that the images are spatially congruent) and 2) differences due to a spatial distortion of one image relative to the other. Let the first, generally nonlinear, relationship between voxel values from the same point (x) in both images be denoted by the operator $f_x\{.\}$ and the distortion by q(x) such that:

$$f_x\{\dagger(x)\} = \Omega(q(x)) + e(x) \qquad (a.1)$$

where e(x) is a normally distributed error term with zero mean. For clarity we will omit the error term and deal with one-dimensional images (generalizing to three-dimensional images at the end of the appendix). Images are assumed to be good lattice representations of the continuous processes $\Omega(x)$ and $\dagger(x)$ in a Euclidean space *x*.

The problem of spatial transformation reduces to finding approximate solutions for $f_x\{.\}$ and q(x) subject to reasonable constraints. The constraint on the operator $f_x\{.\}$ is one of local-stationariness, in the sense that $f_x\{.\}$ does not change very much in a local region. [$f_x\{.\}$ is allowed to vary between remote regions of the images.] The minimal constraint on the spatial transformation q(x) is assumed to be a preservation of local contiguity relationships [i.e., q(x) is a smooth and the associated Jacobian is positive]. We will deal here with the most general case of these minimal constraints.

At first glance Equation (a.1) may appear so ill posed as to make any explicit solution impossible. However, if we assume the images are smooth (or that they can be rendered smooth—see main text) then a first order approximation of Equation (a.1) can be constructed in which both the operator $f_x\{.\}$ and q(x) have a least squares solution. The remainder of this section describes how this is done.

First decompose $f_x\{.\}$ into a convolution and a functional:

$$f_x\{.\} = c(x) * \gamma_x(.) \qquad (a.2)$$

where * denotes convolution. c(x) is a kernel or differential point spread function. Without loss of generality one can take some expansion of $\gamma_x\{.\} = \Sigma\, u_i(x).f^i\{\dagger(x)\}$ where $f^i\{.\}$ could correspond to terms in a polynomial, a Taylor series, a Fourier series, and so on. The local-stationariness constraint on $f_x\{.\}$ can be implemented by expanding the coefficients of $f^i\{.\}$ [i.e., $u_i(x)$] in terms of some "smooth" spatial basis functions $\beta_j^f(x)$:

$$u_i(x) = \Sigma\, u_{ij}\, \beta_j^f(x). \qquad (a.3)$$

q(x) can be similarly expanded in terms of *x* and some smooth basis functions $\beta_k^q(x)$:

$$q(x) = x + \Sigma\, q_k \beta_k^q(x) \qquad (a.4)$$

and

$$\partial q(x)/\partial q_k = \beta_k^q(x). \qquad (a.5)$$

Using these expansions Equation (a.1) becomes:

$$c(x) * \Sigma\, \{f^i(\dagger(x))\, \Sigma\, u_{ij} \beta_j^f(x)\} \approx \Omega(x + \Sigma\, q_k \beta_k^q(x)). \qquad (a.6)$$

If $\Omega(x)$ is smooth the effects of small distortions q_k $\beta_k^q(x)$ will not interact to a significant degree and we can expand the right-hand side of eqn(a.6) using Taylor's theorem where, ignoring high order terms:

$$\Omega(x + \Sigma\, q_k \beta_k^q(x)) \approx \Omega(x) + \Sigma\, q_k \beta_k^q(x).\partial\Omega(x)/\partial x. \qquad (a.7)$$

Equation (a.7) is asymptotically true for small q_k and reasonably true, if $\Omega(x)$ is smooth, for larger q_k. The

right-hand side of Equation (a.7) can be expressed directly in terms of q_k by noting that from Equation (a.5):

$$\beta_k^q(x).\partial\Omega(x)/\partial x = \partial q(x)/\partial q_k.\partial\Omega(x)/\partial x = \partial\Omega(q(x))/\partial q_k \quad (a.8)$$

i.e.,

$$\Omega(x + \Sigma\, q_k\beta_k^q(x)) \approx \Omega(x) + \Sigma\, q_k\partial\Omega(q(x))/\partial q_k. \quad (a.9)$$

This first order approximation [Equations (a.7) or (a.9)] is substituted into Equation (a.6):

$$c(x) * \Sigma\Sigma\,[f^i(\dagger(x)).u_{ij}\beta_j^f(x)] - \Sigma\, q_k\beta_k^q(x).\partial\Omega(x)/\partial x \approx \Omega(x). \quad (a.10)$$

Given the "good lattice" assumption, Equation (a.10) can be expressed in matrix notation as:

$$[\mathbf{c}.\mathrm{diag}(f^0(\dagger)).\boldsymbol{\beta}^f\,\mathbf{c}.\mathrm{diag}(f^1(\dagger)).\boldsymbol{\beta}^f\cdots -\mathrm{diag}(\partial\Omega/\partial\mathbf{x}).\boldsymbol{\beta}^q].[\mathbf{u}_0\,\mathbf{u}_1\cdots\mathbf{q}]^T \approx \Omega$$

or

$$[\mathbf{c}.\mathrm{diag}(f^0(\dagger)).\boldsymbol{\beta}^f\,\mathbf{c}.\mathrm{diag}(f^1(\dagger)).\boldsymbol{\beta}^f\cdots -\partial\Omega/\mathbf{dq}].[\mathbf{u}_0\,\mathbf{u}_1\cdots\mathbf{q}]^T \approx \Omega \quad (a.11)$$

where $\mathbf{c}$ is a Toeplitz matrix of the convolution kernel $c(x)$. $\mathrm{diag}(f^i(\dagger))$ represents a diagonal matrix with leading diagonal elements $f^i(\dagger(x))$ at the location of all voxels. The matrix $\boldsymbol{\beta}^f$ and $\boldsymbol{\beta}^q$ contain a basis function in each column and have the same number of rows as voxels analyzed. $\mathbf{u}_i$ and $\mathbf{q}$ are row vectors of the unknown coefficients. Ω and $\partial\Omega/\partial\mathbf{x}$ are column vectors with one element per voxel. Let:

$$\mathbf{A} = [\mathbf{c}.\mathrm{diag}(f^0(\dagger)).\boldsymbol{\beta}^f\,\mathbf{c}.\mathrm{diag}(f^1(\dagger)).\boldsymbol{\beta}^f\cdots -\mathrm{diag}(\partial\Omega/\partial\mathbf{x}).\boldsymbol{\beta}^q].$$

Then from Equation (a.11)

$$\mathbf{A}.[\mathbf{u}_0\,\mathbf{u}_1\cdots\mathbf{q}]^T \approx \Omega$$

and

$$[\mathbf{u}_0\,\mathbf{u}_1\cdots\mathbf{q}]^T \approx (\mathbf{A}^T.\mathbf{A})^{-1}\mathbf{A}^T.\Omega. \quad (a.12)$$

Equation (a.12) represents the least squares solution of the unknown coefficients $[\mathbf{u}_0\,\mathbf{u}_1\cdots\mathbf{q}]^T$. The elements of these vectors specify the approximations of $f_x\{\cdot\}$ and $q(x)$ in the space defined by the (generally nonlinear) basis functions. The corresponding expressions in three dimensions (x, y, and z) are:

$$\mathbf{A} = [\mathbf{c}.\mathrm{diag}(f^0(\dagger)).\boldsymbol{\beta}^f\,\mathbf{c}.\mathrm{diag}(f^1(\dagger)).\boldsymbol{\beta}^f\cdots -\mathrm{diag}(\partial\Omega/\partial\mathbf{x}).\boldsymbol{\beta}^q] -\mathrm{diag}(\partial\Omega/\partial\mathbf{y}).\boldsymbol{\beta}^q -\mathrm{diag}(\partial\Omega/\partial\mathbf{z}).\boldsymbol{\beta}^q]$$

and

$$[\mathbf{u}\,\mathbf{v}\,\mathbf{q}_x\,\mathbf{q}_y\,\mathbf{q}_z]^T \approx (\mathbf{A}^T.\mathbf{A})^{-1}\mathbf{A}^T.\Omega$$

where [c.f. Equation (a.4)]:

$$q(x) \equiv \mathbf{x} + \boldsymbol{\beta}^q.\mathbf{q}_x \quad (a.13)$$

and similarly for $q(\mathbf{y})$ and $q(\mathbf{z})$. The spatially normalized image $\Omega_n(x, y, z)$ is simply:

$$\Omega_n(x, y, z) = \Omega(q(x), q(y), q(z)). \quad (a.14)$$